Journal of Materials Chemistry C

ROYAL SOCIETY OF CHEMISTRY

REVIEW

View Article Online
View Journal | View Issue

Cite this: J. Mater. Chem. C, 2022, 10, 2431

Recent progress in open-shell organic conjugated materials and their aggregated states

Shaoqiang Dong[a] and Zhen Li *[abc]

In the last few decades, open-shell organic materials have attracted great attention from scientists due to their new chemical and physical properties, as well as their possible applications in new-generation organic light-emitting diodes (OLEDs), organic field effect transistors (OFETs), organic spintronics and photonics, and so on. In this review, we summarize the recent progress in the design and synthesis of open-shell organic conjugated materials. First, we give a general summary of synthetic strategies towards these stable open-shell species, such as kinetic steric protections, spin delocalization by large π-conjugated skeletons and heteroatom-assisted protections. In particular, we will focus on their aggregated states in OFETs, organic conductors, luminescent devices and photoinduced radical materials, with the aim to provide some clue for the further development of novel open-shell organic conjugated materials.

Received 25th September 2021,
Accepted 19th November 2021

DOI: 10.1039/d1tc04598a

rsc.li/materials-c

1. Introduction

Different from traditional organic semiconductor materials, open-shell organic materials have emerged as a new generation of organic electronic materials due to their unique magnetic properties,[1–26] with great potential in flexible organic electronics,[17,22] organic photonics,[19–22] spintronics[16,23] and organic quantum devices[27] in the last few decades. Since they are usually related to organic small molecules, oligomers, dendrimers or polymers with unpaired electrons, open-shell organic materials could also be called organic radicals. And, according to the number of unpaired electrons, organic radicals could be classified as organic monoradicals, diradicals, triradicals and other high-spin organic radicals.[6]

Organic molecules with one unpaired electron are called monoradicals (Fig. 1a), in which one unpaired electron possesses a magnetic moment and a spin quantum number of $S = 1/2$ with magnetic components $m_s = +1/2$ and $m_s = -1/2$. Once an external magnetic field (H) is applied in a certain direction, the magnetic moment of the electron will align either ($m_s = -1/2$, β spin) parallel or antiparallel ($m_s = -1/2$, α spin) to the field. Therefore, the spin multiplicity ($2S + 1$) of the monoradicals is doublet (2) and the monoradicals could also be called doublet radicals. Each electron's magnetic moment possesses a specific energy due to the Zeeman effect, and this energy could be described as the equation of $E = m_s g_e \mu_e H$, among which g_e is called the g factor, μ_e is the Bohr magnetron and H is the strength of the applied magnetic field. For monoradicals, the Zeeman energy difference between the lower and upper states of two electrons is calculated to be $\Delta E = E_\alpha - E_\beta = g_e \mu_e H$, and the electron spin resonance (ESR) signal would appear when its frequency (ν) is equal to the energy of $\Delta E = h\nu$.

Diradicals are related to molecules with two unpaired electrons. There are three cases. As shown in Fig. 1b, when the distance (r) of two electrons is large enough, the electron exchange interaction (J) of two unpaired electrons could be regarded as almost negligible, and this kind of radical could be named as a biradical with two doublet monoradicals in one molecule. However, when the distance (r) of two electrons is small enough to generate spin–spin interactions, the electron exchange interaction would produce two spin states of singlet diradicals ($S = 0$, spin multiplicity = 1) and triplet diradicals ($S = 1$, spin multiplicity = 3). For singlet diradicals, the quantum number is zero and spin multiplicity is one, indicating only one energy level. Thus, singlet diradicals are ESR silent. For triplet ones, the quantum number is 1, $\alpha\alpha$ ($m_s = +1$), $\alpha\beta$ ($m_s = 0$), $\beta\beta$ ($m_s = -1$), and spin multiplicity is 3. Thus, there are three different energy levels in the presence of a strong magnetic field, and triplet diradicals are ESR-active species. Usually, singlet diradicals have small singlet–triplet band gaps (ΔE_{S-T}), and these molecules are easy to thermally activate to their triplet states. Accordingly, temperature-dependent magnetic measurements are commonly used methods to determine singlet diradicaloids. For example, the protons of singlet

[a] Institute of Molecular Aggregation Science, Tianjin University, Tianjin 300072, China. E-mail: lizhentju@tju.edu.cn
[b] Hubei Key Lab on Organic and Polymeric Opto-Electronic Materials, Department of Chemistry, Wuhan University, Wuhan 430072, China. E-mail: lizhen@whu.edu.cn
[c] Joint School of National University of Singapore and Tianjin University, International Campus of Tianjin University, Binhai New City, Fuzhou 350207, China

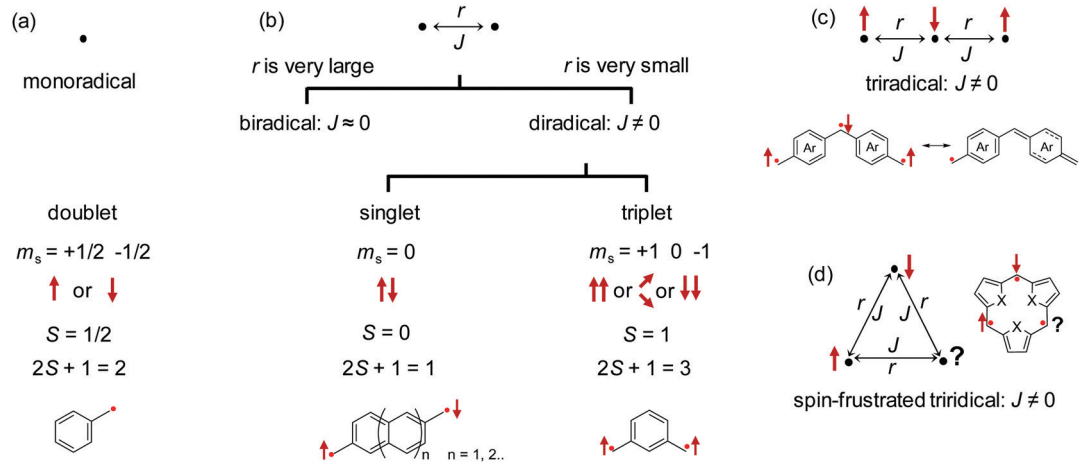

Fig. 1 Schematic graphs of a (a) monoradical, (b) biradical and diradical, (c) triradical, and (d) spin-frustrated triradical. *r*: the distance between two electrons: *J*: electron exchange integral: m_s: magnetic components: *S*: spin quantum number; (2*S* + 1): spin multiplicity.

diradicals in ^{1}H NMR spectra would be broadened upon heating, and the product of magnetic susceptibility and temperature would also increase as the temperature increases, which could be monitored by variable temperature ESR or superconducting quantum interfering device (SQUID) measurements.

Triradicals and above are called high-spin radicals only when *J* not equal to zero is considered.[6,9] Taking triradicals for example (Fig. 1c), if three radicals align in a linear lattice, one of the radicals will remain unpaired due to the electron coupling of two neighbour radicals. Therefore, the linearly aligned triradical would usually have the doublet ground state of the monoradical. If three radicals align in a triangular lattice with arbitrary, and two of them have opposite spin states (Fig. 1d), the third spin could not align itself to satisfy both of them at the same time. In other words, the energies of the two systems would be the same, no matter whether the third electron is in the spin up or down state. Therefore, the two spin states of the third electron have the same probability, and this kind of triradical is called a spin-frustrated triradical.[27–30] In the solid state, due to the random frozen states of their spin states, the magnetic susceptibility is zero macroscopically, and this triradical could be called a spin glass material. However, when applying/removing the external magnetic field, the triradical would be slowly magnetized/demagnetized and exhibit hysteresis phenomena. Triangular triradicals have shown great potential applications in molecular storage and organic quantum devices, benefiting from their unique magnetic properties; however, this kind of triradical has been rarely reported.

2. Synthetic strategies towards stable organic open-shell materials

Since the discovery of persistent stable triphenylmethyl radical **1** with its dimer **2** at equilibrium in solution by Gomberg early in 1900,[31] scientists have been always developing synthetic strategies towards stable organic open-shell materials. As shown in Fig. 2, triphenyl chloromethane was dissolved in benzene, and **1** could

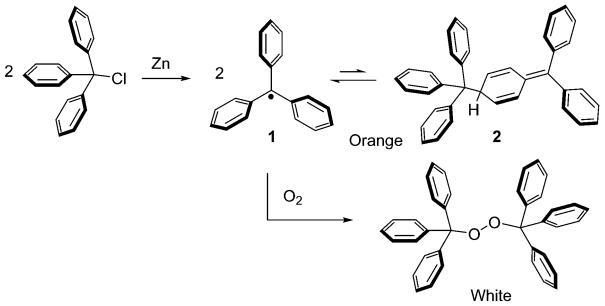

Fig. 2 Triphenylmethyl radical and its derivatives.

be synthesized upon the addition of Zn powder with the appearance of orange color. The color would fade immediately once exposed to air with the formation of white peroxide, indicating the high reactivity and instability of monoradical **1**.

2.1 Kinetic steric protection by bulky substituents

Steric protection is a commonly used and effective strategy towards air stable organic open-shell molecules.

Taking monoradical **1** for example, the introduction of bulky substituents on the neighbour positions in the phenyl rings of **1** would sterically protect the monoradical on α-carbon and prevent its dimerization reaction. Furthermore, the steric hindrance would also compel the phenyl rings to distort to a certain angle, and reduce the possibility of spin distribution expanding to the *para* positions of the phenyl rings. Therefore, hexamethoxyl substituted monoradical **3** (Fig. 3) could be stable in the solid state, and react with oxygen in air very slowly.[32] Multi-chlorinated organic monoradicals **4–5** are thermally stable in air, which could be stored in air for several months.[33] Recently, Li, Kusamoto and Nishihara demonstrated the possible application of these monoradicals in next-generation organic light-emitting diode (OLED) materials.[22,34–36] In 2018, Kubo *et al.* reported air-stable highly congested tri(9-anthryl)methyl monoradical **6a** with an unpaired electron

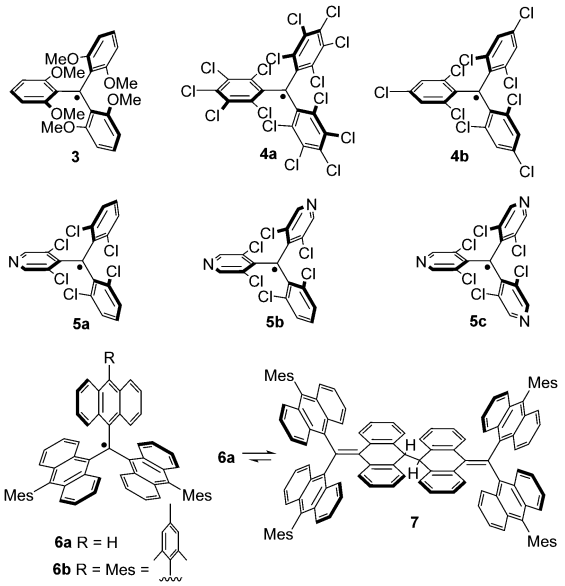

Fig. 3 Representative monoradicals with steric protections.

mainly localizing on the central carbon. However, if the 10-position of one anthracene is not protected by the mesityl group, a tail-to-tail dimer **7** would be isolated instead, rather than the head-to-tail dimer **2**.[37] Further thermodynamic analysis revealed the much larger equilibrium constant of **6b** and its dimer **7** with a log K_D of 6.69 at 198 K, in comparison with that of **1** and its dimer **2** with a log K_D of −3.48.

Similarly, steric protections could also be used to protect diradicaloids. As shown in Fig. 4, early in 1904, diphenylmethylene terminated quinoidal *p*-quinodimethane (*p*-QDM) **8** was synthesized by Thiele, and also named Thiele's hydrocarbon,[38] which possesses a closed-shell ground state.[39] Its extended structure, compound **9**, was synthesized by Tschitschibabin later in 1907 and therefore called Chichibabin's hydrocarbon.[40] However, the high reactivity of **9** towards oxygen caused the impurity problem and made its ground state controversial. Until 1986, Montgomery prepared pure **9** in an inert atmosphere, and the X-ray crystallographic analysis elaborated its quinoidal structure with a significant diradical character.[39] Recently, Wu and coworkers reported mesityl substituted Chichibabin's hydrocarbon **10** with much improved stability, which allowed the intramolecular dynamics to be conducted. For example, variable-temperature NMR measurements revealed that the rotation energy barrier of **10**-*trans* and **10**-*cis* is 11.40 kcal mol^{-1}.[41]

The contribution of the open-shell resonance form to the ground state could be described by the biradical character index *y*. When $y = 1$, it indicates a pure diracialoid; when $y = 0$, it indicates a closed-shell structure. Conjugated extended fused quinoidal *p*-QDMs are predicted to be diradicaloids with high diradical characters.[10,15,16] Therefore, different substitution strategies were utilized to develop stable 2,6-anthraquinodimethane (*p*-AQDM) containing compounds **11–14** (Fig. 4). Compound **11** ($y = 0.68$ at the CASSCF(2,2)/6-31G level) with four phenyl substituents developed by Kubo in 2012 could only be stable in air for a couple of days.[42] Extended nonazethrene **12** ($y = 0.25$

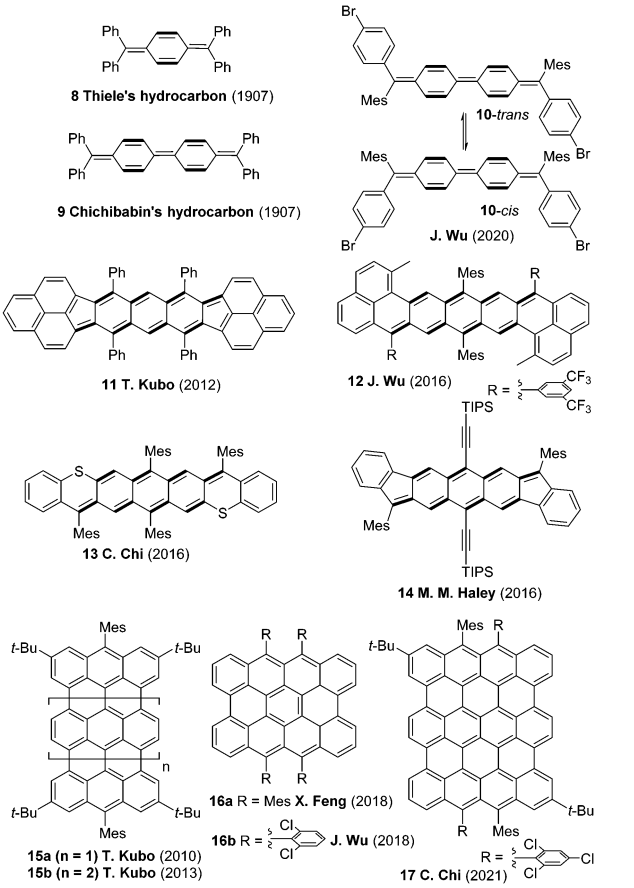

Fig. 4 Representative diradicaloids with steric protections.

at the RAS-SF/6-31G(d,p) level) with two mesityl groups and two electron-withdrawing groups developed by Wu could only show a half-life of 16 h.[43] In contrast, compound **13** (0.381 at the UCAM-B3LYP/6-31G level), a S-atom containing acene analogue, developed by Chi and coworkers with four mesityl groups, exhibited excellent photostability with a half-life longer than one month.[44] Extended indofluorene **14** (0.381 at the PUHF level) synthesized by Haley with triisopropylsilyl (TIPS) ethynyl substituents and two mesityl groups showed a half-life of 64 days in solution.[45]

Recently, scientists found that steric protection strategies showed great influence on the stabilization of extremely challenging extended [*n*, *m*]peri-acenes. As shown in Fig. 4, Kubo *et al.* reported **15a** and **15b** with a diradical character of 0.54 and 0.91 (at the CASSCF(2,2)/6-31G level), respectively.[46,47] However, these molecules could be stabilized by introducing bulky mesityl groups to the reactive zigzag edges and four *tert*-butyl groups. The half-life of **15a** was reported to be 3 days even after being exposed to air, while the non-mesityl derivative of **15a** decomposed instantly in an inert atmosphere.[46] For zigzag-edge extended **16a**, the decay curve of absorption spectra gave its half-life of 15 hours in air and under ambient light.[47] Feng and Wu's groups independently reported the laterally extended [4, 2]peri-acene derivatives **16a** (0.72 at the PUHF level) substituted by two mesityl and two 4-*tert*-butylphenyl groups,[48]

and **16b** (0.515 at the UCAM-B3LYP/6-31G level) protected by four 2,6-dichlorophenyl groups,[49] respectively. **16a** only showed persistent stability with a half-life of 3 h, while **16b** had a half-life of 7 h, indicating the better protection of 2,6-dichlorophenyl groups. Very recently, Chi *et al.* reported the vertical extended [4, 3]peri-acene **17**.[50] Surprisingly, even its diradical character was calculated to be 0.948, approaching a pure diradical. However, **17** showed much better stability even than **16a** and **16b** with a half-life of 157 h. This could be ascribed to the bulky and electron-withdrawing 2,4,6-trichlorophenyl groups at the reactive zigzag edges, together with the additional two *tert*-butyl groups.

2.2 Spin-delocalization by organic π systems

Another important strategy to realize stable organic open-shell materials is to utilize the delocalization of radical electrons on organic π systems to dilute the spin density of organic open-shell molecules and consequently decrease their reactivity.

As shown in Fig. 5, **18a–c** are typical pentaphenylcyclopentadienyl radicals, and radical electrons could be delocalized on the cyclopentalienyl ring.[51–53] Among them, **18c** is the only air-stable monoradical due to the delocalization of TIPS ethynyl substituents.[52] The fluorenyl radical could be regarded as a dibenzo fused cyclopentalieny radical, and according to DFT calculation results, spin electrons could delocalize on the whole fluorene. Therefore, by well protecting the 3,6,9-positions with bulky substituents, Wu *et al.* reported air-stable fluorenyl radical **19**, which could be isolated even by common column chromatography on silica gel.[54,55]

Phenalenyl **20a** is a typical representative monoradical hydrocarbon with odd carbon numbers.[56–58] Due to its high reactivity, it could not be stable in air. However, three *tert*-butyl substituted phenalenyl **20b** could be stable and can form a π–π stacked dimer in the crystal state under low temperatures.[56] Kubo *et al.* reported cyclopentalienyl linked two phenalenyl derivative **21**, which exhibited excellent air stability with a half-life of 60 h. Interestingly, since **21** only has one *n*-butyl substituent, its stability obviously benefitted from the delocalization on the whole π system.[59] Recently, Sun *et al.* reported air-stable olympicenyl radical **22** protected by the TIPS ethynyl substituent with a long half-life of 7 days. Further study indicated that **22** could form a head-to-tail dimer with a unique 20-center-2-electron structure in the solid state, and the ground state of π-dimers was found to be singlet diradicaloid.[60]

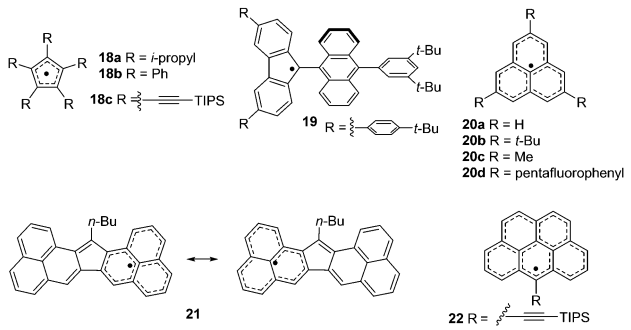

Fig. 5 Representative monoradicals stabilized by spin-delocalization.

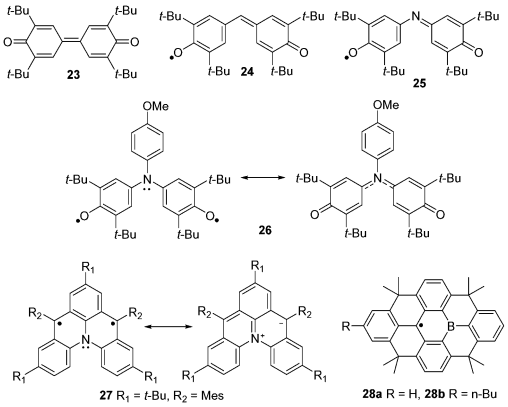

Fig. 6 Representative open-shell molecules stabilized by heteroatoms.

2.3 Heteroatom (B and N atoms) assisted open-shell molecules

Heteroatoms could be utilized to stabilize open-shell molecules, including heteroatom-centre radicals and heteroatom-assisted open-shell molecules for their interesting electronic structures. And, we will emphasize the latter one focusing on the bridge-linking effect of heteroatoms (B and N atoms) on open-shell species through their *p*-orbitals.

Compound **23**, the quinone analogue of Chichibabin's hydrocarbon shown in Fig. 6, possesses a closed-shell ground state. And **24**, first synthesized by Galvin M. Coppinger in 1957 and also called a galvinoxyl radical, could be regarded as a methane-inserted structure of **23**.[61] Due to the formation of a quinoidal structure by one of the phenoxy radicals and the unpaired *p* electron of methane carbon, **24** shows the doublet ground state of a monoradical. Similarly, its isoelectronic structure **25** with imine nitrogen atoms was also reported to be a monoradical.[62] Seki *et al.* reported an amine nitrogen linked two phenoxy radicals **26**, and X-ray crystallographic analysis reveals the C–N bonds with multiple-bond characters, indicating the effective conjugation between two phenoxy radicals through the *p*-orbital of the amine N atom. Interestingly, the ground state of **26** possesses a closed-shell singlet electronic state even at 388 K.[63]

Shimizu *et al.* reported azoniadibenzo[*a*,*j*]phenalenide **27** (Fig. 6) with a singlet diradical ground state.[64] Further study indicates its zwitterion structure with negative charge delocalized over the periphery of the molecule and positive charge mainly localized near the nitrogen atom. Yamagushi *et al.* reported a B containing monoradical **28** with spin density effectively delocalized through the vacant *p*-orbital of the boron atom.[65] Therefore, **28** is an air-stable monoradical exhibiting well balanced ambipolar carrier transport properties.

3. Aggregated open-shell organic materials in organic semiconductors

Open-shell organic conjugated materials usually exhibit special charge-transport properties, which is different from traditional

organic semiconductors due to their unique physical properties, such as unique electronic structures and aggregated structures, and temperature-dependent magnetic properties.

3.1 Polycyclic conjugated open-shell diradicaloids

By adjusting the substituents of indenofluorene, Haley *et al.* found that a single crystal device of compound **29** (Fig. 7) with two pentafluorophenyl groups showed a hole/electron carrier mobility of $7.0 \times 10^{-4}/3.0 \times 10^{-3}$ cm^2 V^{-1} s^{-1}, respectively.[66] Later in 2016, Haley reported that diradicaloid **14** (Fig. 7) also showed a balanced ambipolar carrier transport character with a hole/electron carrier mobility of $2.0 \times 10^{-3}/4.0 \times 10^{-3}$ cm^2 V^{-1} s^{-1}, respectively.[45] The relatively low charge transport mobility could be ascribed to the introduction of bulky substituents, which is beneficial for the stability of diradicaloids but harmful for the effective molecular π–π packing and charge transport.

To enhance the π–π overlap of neighbour molecules, Haley *et al.* reported lateral extended indenofluorene derivatives **30–32**.[67] X-ray crystallographic analysis indicates the influence of chemical structure modifications on crystal packing. As shown in Fig. 8a, b, e and f, **30a** and **30b** with larger bulky substituents show disconnected 1D π–π packing, while **32** arranges in dimers and there are no π–π or C–H···π interactions between neighbour dimers. Therefore, no FET character could be detected for **30a**, **30b** and **32**. It is claimed that both **30c** and **31** crystallize in a two-dimensional (2D) π–π stacking motif, which is known for TIPS-pentacene with superior electrical properties. Therefore, OFET devices of **30c** and **31** based on crystalline thin films exhibit an excellent *p*-type hole mobility of $1.04 \pm 0.68/4.72 \pm 1.97$ cm^2 V^{-1} s^{-1}, respectively. However, the 2D crystal packing of **30c** and **31** described here is not consistent with their previous results, which remain controversial.

Kubo *et al.* reported compound **33** (Fig. 7) with a singlet diradical character of 0.68 at the CASSCF(2,2)/6-31G level and a low optical band gap of 1.1 eV.[68] Its relative high-lying highest occupied molecular orbital (HOMO) energy level and low-lying LUMO energy level make it suitable to exhibit ambipolar carrier transport character. As shown in Fig. 9a and b, **33** packs in one-dimensional (1D) column with a slipped stacking motif and an average π–π distance of 3.137 Å, which is much shorter than the common van der Vaals contact of two sp^2 carbon atoms, indicating its possible fast charge-transport properties.

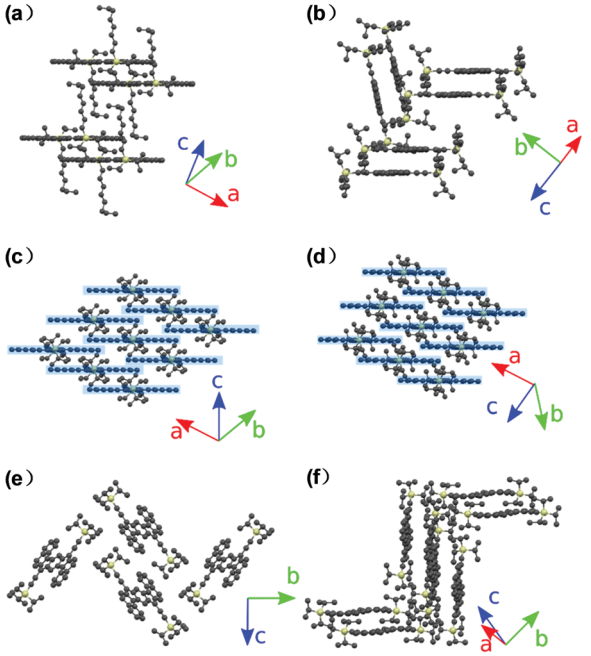

Fig. 8 Solid-state packing for **30–32**: (a) **30a**, (b) **30b**, (c) **30c**, (d) **31**, (e) **32** along a direction, and (f) **32** viewed down the long axis of the backbone. Adapted with permission from ref. 67, Copyright 2019, American Chemical Society.

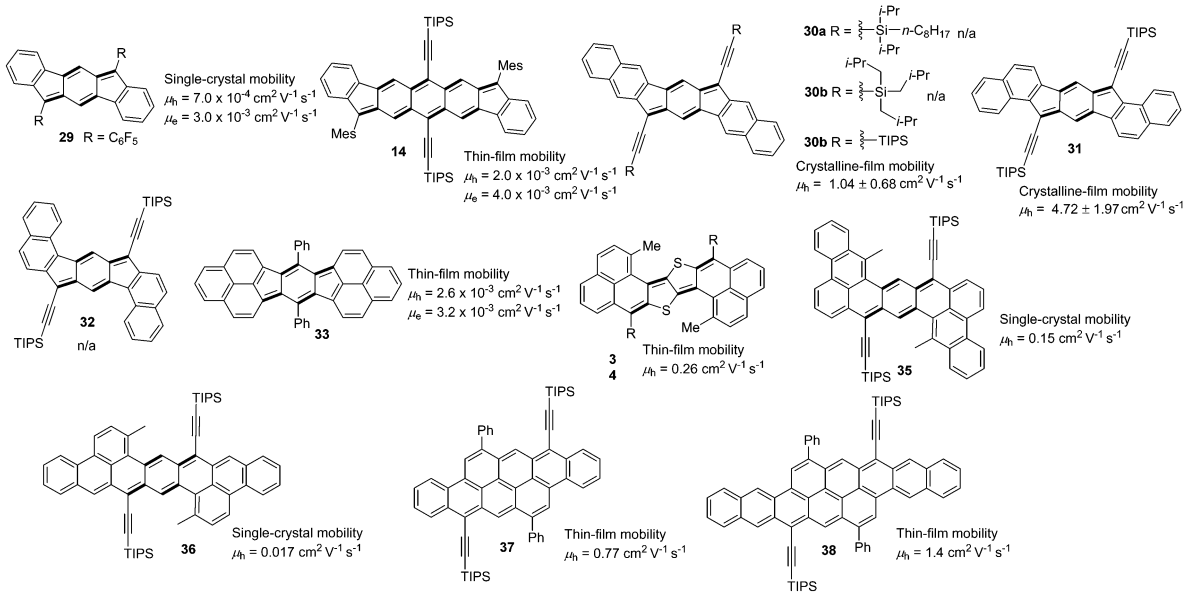

Fig. 7 Open-shell diradicaloids for organic electronics.

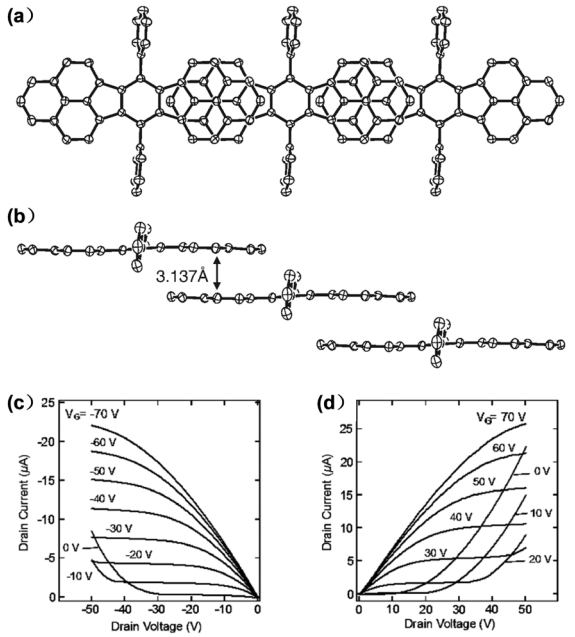

Fig. 9 Packing motifs of **33** in the crystal structure with (a) top view and (b) side view. Hydrogen atoms and the solvated chlorobenzene molecule are omitted for clarity. Output characteristics of the ambipolar OFET based on Ph2-IDPL for (c) negative and (d) positive gate biases. Adapted with permission from ref. 68 and 69. Copyright 2005, Wiley-VCH Verlag GmbH & Co and copyright 2007, AIP Publishing.

However, the electrical conductivity of **33** has a value of 5.0×10^{-5} S cm^{-1}. Furthermore, the thin-film OFET device shows its balanced hole/electron mobility of 2.6×10^{-3}/3.2×10^{-3} cm^2 V^{-1} s^{-1}, respectively.[69]

Bisphenaleno-thieno[3,2-*b*]thiophene **34** (Fig. 7) was developed by Chi's group.[70] X-ray crystallographic analysis reveals its typical quinoidal resonance form with an unexpected wave-shape structure due to the strong intermolecular phenalenyl-phenalenyl π–π interactions in crystals. DFT calculations indicate its diradical charater of 0.186 (at UCAM-B3LYP/6-31G level), which probably originated from the thermodynamic stabilizing effect of the delocalized phenalenyl moieties. In addition, its OFET devices based on solution processed thin films exhibit *p*-type operation with a mobility of 0.26 cm^2 V^{-1} s^{-1}. Very recently, Sun and Li reported two isomeric dibenzo extended heptazethrenes **35** and **36** with moderate diradical characters of 0.11 and 0.13 (at the UCAM-B3LYP/6-31G level), respectively.[71] X-ray crystallographic analysis reveals their dimeric structures with one molecule periodically aligned in the crystal. Although no obvious 1D or 2D π–π stacking motifs were observed, top-contact bottom-gate OFETs based on single crystals of **35** and **36** give the highest hole mobilities of 0.15 cm^2 V^{-1} s^{-1} and 0.017 cm^2 V^{-1} s^{-1}, respectively.

Extended acenes with a significant diradical character for OFETs are rarely reported, as limited by their poor stability.[72] Frigoli *et al.* reported slipped bisacene compounds **37** and **38** with a diradical character of 0.50 and 0.64 (at the UHF/6-31G(d, p) level), respectively. However, **37** and **38** showed a long half-life of 6.5 and 4.9 days, respectively. The excellent stability allows their thin-film OFET devices to be fabricated, with a mobility of up to 0.77 cm^2 V^{-1} s^{-1} and 1.4 cm^2 V^{-1} s^{-1} for **37** and **38**, respectively.

3.2 Tetracyano terminated open-shell diradicaloids

Tetracyano terminated *p*-QDMs could serve as *n*-type semiconductors due to their low-lying LUMO energy levels caused by the strong electron-withdrawing effect of the terminal group and planar conjugated structures favourable for solid packing and charge-transport in organic electronics.

Tetracyano terminated π-extended quinoidal structures would also show an increased diradical character.[15] As shown in Fig. 10, in 2005, Otsubo *et al.* reported compounds **39a–f** with up to six quinoidal thiophene rings by fusing the β-positions of each thiophene ring with bis(butoxymethyl)cyclopentane substituents. Further experimental and DFT calculated results reveal that molecules longer than **39c** (n = 3) show a gradually increased open-shell singlet diradical ground state accompanied by the extension of quinoidal oligothiophenes.[73] In 2007, by reducing two bulky substituents, Takimiya *et al.* reported the n-type charge transport properties of **40** with a mobility of 0.16 cm^2 V^{-1} s^{-1}, revealing their potentials in *n*-type semiconductors.[74]

Tetracyano terminated cyclic fused compound **41** reported by Li and coworkers displayed *n*-type FET behaviour with an electron mobility of up to 0.9 cm^2 V^{-1} s^{-1} under ambient conditions, which is beneficial for its low-lying LUMO energy level (−4.3 eV).[75] In 2014, Takimiya *et al.* reported the synthesis and characterization of two regioisomers **42** and **43** with moderate electron mobilities of 3.2×10^{-3} cm^2 V^{-1} s^{-1} and 1.4×10^{-3} cm^2 V^{-1} s^{-1}, respectively.[76] It is worth noting that the low-lying LUMO energy levels around −4.6 eV enable their stable operation in n-channel OFETs under ambient conditions. Later, they further synthesized another regioisomer **44a**,[77] which showed significantly red-shifted absorption for its up-shifted

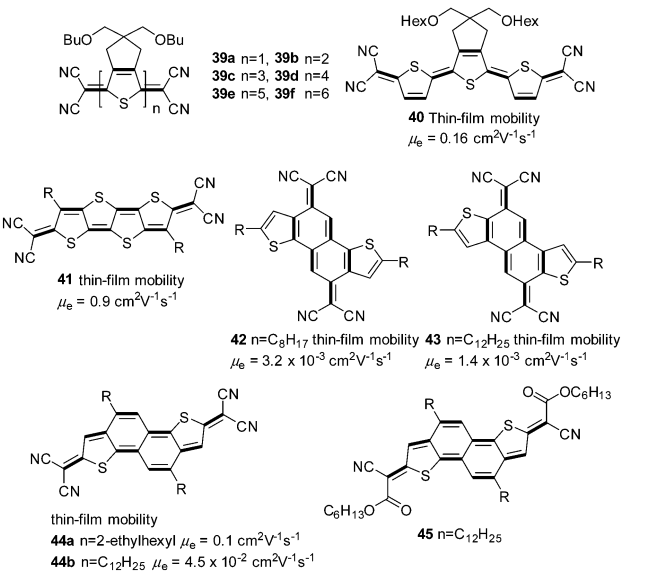

Fig. 10 Chemical structures of tetracyano terminated *p*-QDMs.

E_{LUMO} values compared to that of **42**. Furthermore, **44a** showed a moderately high electron mobility of 0.1 $cm^2 V^{-1} s^{-1}$. However, all these compounds were studied as semiconductors, and their ground states were not well investigated.

By changing capping groups, in 2016, Takimiya and Casado reported the ((alkyloxy)carbonyl)cyanomethylene groups capped quinoidal naphthodithiophene **45**, which could undergo reversible diradical σ-dimerization/σ-polymerization triggered by mild stimuli such as solution concentration, temperature and pressure.[78] The reaction reversibility was caused by the quinoidal molecule **45**, which could change its structure to aromatic species by forming weak and long intermolecular C–C single bonds (Fig. 11a and c). The two opposite but complementary quinoidal and aromatic tautomers provided two Janus faces of the reactants and products, which caused the huge chromic effect of about 2.5 eV. However, no such changes were detected for the quinoidal naphthodithiophene **44b** with dicyanomethylene terminal groups, since it can only form π-dimers (Fig. 11b). The reversible reactions of **45** reveal an unusual mechanism of weak covalent supramolecular bonding, which provides a typical model to understand the fundamental properties of the diverse aggregated modes of π-conjugated diradicaloids.

4. Aggregated open-shell organic materials in one-component organic conductors

Organic conductors have been studied for more than 60 years. To realize the organic metallic state with good conductivity, it usually requires three basic conditions: (1) the existence of unpaired electrons; (2) a solid structure with charge transport channel and effective delocalization of unpaired electrons in a metallic band; (3) weak electron–electron Coulomb repulsive interactions.[79]

Early in 1973, the charge-transfer complex TTF-TCNQ (Fig. 12) was obtained as a metallic molecular crystal with a

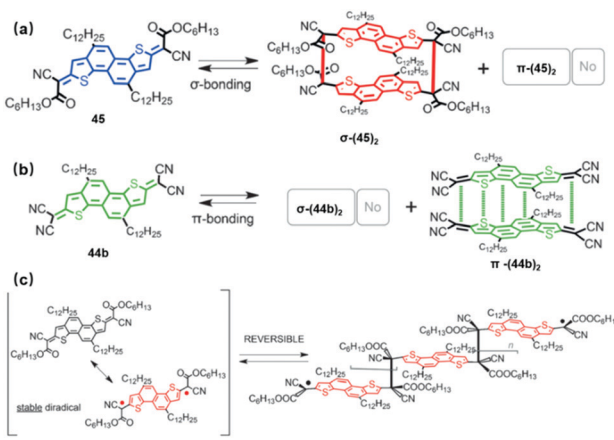

Fig. 11 (a) Reversible σ-dimerization of 45; (b) reversible π-dimerization of **44b**; (c) reversible σ-polymerization of 45. Adapted with permission from ref. 78. Copyright 2016, Wiley-VCH Verlag GmbH & Co.

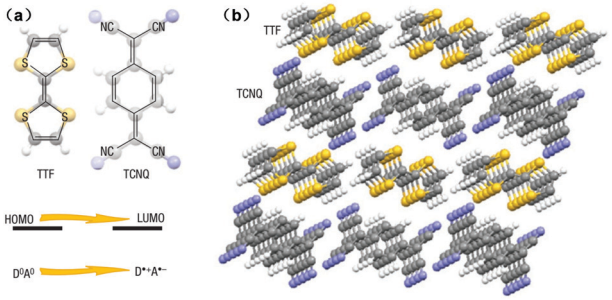

Fig. 12 (a) Chemical structures of TTF and TCNQ; (b) quasi-1D chain like segregated stacking motifs in TTF and TCNQ. Copyright 2008, Springer Nature.

conductivity of 10^2 S cm^{-1}.[80,81] The formation of a radical cation and radical anion by charge transfer and the corresponding partially filled band structure generated from the mixed valence state contribute to the conducting behaviour of TTF-TCNQ salts.

4.1 Open-shell organic diradicaloids for conductors

One component diradicaloids usually have semiconductor characteristics as described above. Recent studies demonstrated that dicyanomethylene capped π-extended quinoidal structures could exhibit self-doping behaviour and consequent intrinsic conducting properties.[24]

1,2,4-Benzotriazinyl radicals (**46**, Fig. 13), which could also be called Blatter radicals, have attracted scientists' attention due to their interesting magnetic and electronic properties, and especially their exceptional air and moisture stability.[82] In 2015, Wudl's group synthesized benzotriazinyl diradicaloids **47a** with a small optical energy gap of around 1.20 eV. The sharper and new extra peaks observed upon cooling in VT ^{1}H NMR spectra indicated its singlet diradical ground state. However, further ESR studies on the polycrystalline solid demonstrated an intermolecular quintet state at room temperature.[83]

The followed work by cooperation of Wudl and Nguyen revealed the unprecedented self-doping behaviour of **47a** and **47b**, involving a radical anion–radical cation pair.[84] Moreover, the number of radical anion–radical cation pairs of **47a** and **47b** was found to be temperature dependant and reversible, indicating that the phenomenon was not originated from oxygen doping. To further confirm the enhanced doping strength with the increasing temperature, OFET devices were fabricated by doping **47a**/**47b** with the strong electron acceptor 2,3,5,6-tetrafluoro-7,7,8,8-tetracyanoquino-dimethane (F4TCNQ). It was found that transfer curves were insensitive to the F4TCNQ concentration, with I_d all exhibiting a flat response to V_g. Interestingly, the transfer curve of pristine **47a** at 370 K in a high V_g region almost

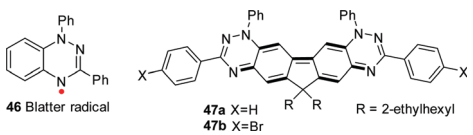

Fig. 13 Chemical structures of a Blatter radical and derivatives.

overlapped with that of the F4TCNQ doped OFET at 300 K, which helped to confirm the temperature-enhanced self-doping and electrical conductivity in both systems.[84] To our knowledge, this is the first example for diracialoids exhibiting self-doping phenomena, regardless of the low conductivity of 1.06×10^{-4} S cm^{-1}.

In 2018, Zhu *et al.* reported **48a** and **48b** with dicyanomethylene capped two-dimensional extended quinoidal oligothiophene structures.[85] Electrochemical measurements revealed their surprisingly narrow band gaps of 0.67 and 0.65 eV for **48a** and **48b**, respectively. DFT calculations (at the UCAM-B3LYP/6-31G level) revealed their diradical character of 0.49 and 0.52, respectively. The singlet and triplet band gaps were calculated to be −3.73 kcal mol^{-1} (0.16 eV) and −3.56 kcal mol^{-1} (0.15 eV) for **48a** and **48b**, respectively, which allowed them to generate thermal activated triplet species. It was clear that the special energy levels of two diradicaloids enabled the possible promotion of free carriers by thermal activation. And, the electrical conductivities of **48a** and **48b** were further measured to be 0.0080 and 0.29 S cm^{-1}, respectively. Later, Zhu *et al.* reported a series of quinoidal molecules **49a–49d**.[86] From dimer to pentamer, DFT calculations showed their increased diracical character of 0.00 (**49a**), 0.02 (**49b**), 0.22 (**49c**) and 0.46 (**49d**), revealing that the ground state changed gradually from closed-shell states to open-shell states. Single component electrical measurements demonstrated that **49a** and **49b** showed a typical semiconductor character, and in contrast, **49a** and **49b** exhibited conductor behaviour with conductivities of 1.5×10^{-4} S cm^{-1} and 3.0×10^{-4} S cm^{-1}, respectively. The formation of free carriers here could also be explained by thermal activation through the narrow bandgaps of extended quinoidal diradicaloids. Interestingly, from **49a** and **49d**, the gradually changed aggregation mode was also observed by AFM and GIWAXS characterization. As shown in Fig. 14b, **49b** had a slipped π–π stacking. However, **49c** (Fig. 14c) showed a cholesteric-like π–π arrangement with a 3.7 Å of intermolecular distance and a 30° average rotating angle between neighbour molecules. For **49d**, the possible σ-polymerization in the solid state with the formation of C–C bonds between neighbour terminal methylene carbons was predicted to be formed due to the relative high diradical character of **49d**.

Guo *et al.* reported the two dicyanomethylene capped imide-bridged fused quinoidal oligothiophene **50** and **51**.[87] The incorporation of a strong electron-withdrawing imide group into the tetracyano-capped oligothiophene backbones ensured their deep LUMO levels (−4.58 to −4.69 eV **50** and **51**, respectively), and the remarkable ambient stabilities of the diradicaloids with half-lives longer than two months. DFT calculations (ωB97XD/6-31G**) indicated that the diradical characters of **50** and **51** were 0.37 and 0.67, respectively. Furthermore, **51** exhibited a cross-conjugation assisted self-doping in the film state (Fig. 15b), which could be confirmed by XPS and Raman studies. Accordingly, **51** exhibited a high electrical conductivity of 0.34 S cm^{-1}, which is among the highest values in single-component organic radical-based conductive materials.

4.2 One-component organic monoradicals for conductors

In principle, one-component neutral monoradicals are ideal building blocks for organic conductors and spintronics.

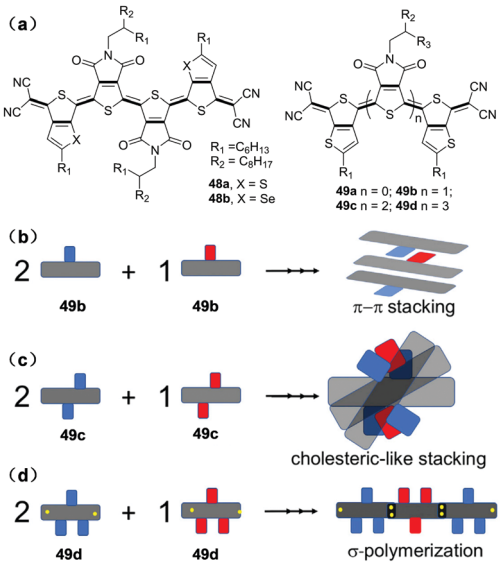

Fig. 14 (a) Chemical structures of dicyanomethylene capped quinoidal oligothiophenes and the possible aggregation modes of (b) **49b**, (c) **49c** and (d) **49d** in the solid state. Copyright 2019, Elsevier.

In practice, however, monoradicals usually show poor conductivities even if 1D π–π stacking charge transport channel could be formed. This should be ascribed to the conduction barrier limited by the on-site neighbour Coulomb repulsion (U, Mott insulator) of relative localized monoradicals.[79] The electronic structure of monoradicals in solid states could be depicted as a half-filled band Mott–Hubbard model. To generate conductivity, the key issue is to realize the equation of $W > U$, where $W = 4\beta$, W is the electronic bandwidth, and β is the intermolecular

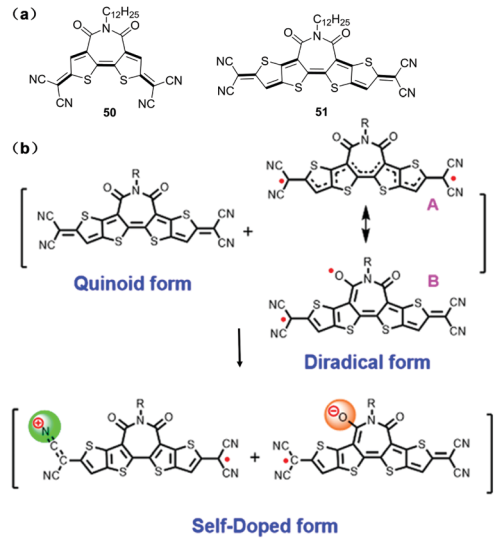

Fig. 15 (a) Chemical structures of **50** and **51**, and (b) proposed self-doping mechanism of **51** through the formation of intermolecular charge transfer species, the fundamental species of the organic conductive compounds. Adapted with permission from ref. 87, copyright 2020, American Chemical Society.

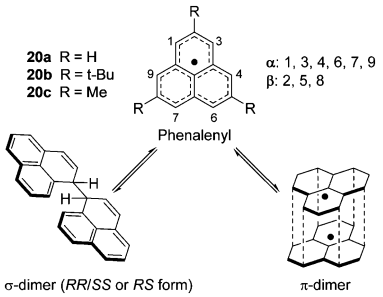

Fig. 16 Dimerization modes of **20**. Copyright 2016, American Chemical Society.

resonance integral. By maximizing W and minimizing U, a metallic state would occur.

For all-carbon centre monoradicals with delocalized spin density, such as phenalenyl **20** (Fig. 16), two dimerization modes, including σ-dimer and π-dimer, were usually observed.[88] The σ-dimer showed a closed-shell ground state for the formation of a new C–C bond accompanied by several stereoisomers, whereas the π-dimer formed a 12-center-2-electron complex with a singlet diradical ground state. Due to the high reactivity of unsubstituted phenalenyl, **20a** has never been reported, while both the σ-dimer and π-dimer of trimethyl substituted **20b** were successfully isolated in the crystalline form.[58] **20c** with three steric *t*-butyl groups could form a π-dimer in the crystal; however, bulky substituents prevented the effective interactions between neighbour dimer pairs.[56] **20d** with three pentafluorophenyl substituents could form 1D π–π stacking columns with an interplanar distance of 3.503 Å; however, the measured conductivity of compressed pellets was only 1×10^{-10} S cm^{-1}, revealing its intrinsic insulator character.

Haddon *et al.* reported a series of spiro-biphenalenyl radicals exhibiting remarkable conductivity by substituent engineering. As shown in Fig. 17, in 1999, Haddon *et al.* reported the first spiro-biphenalenyl monoradical **52e** without bulky substituents, which could be regarded as an intramolecular zwitterionic structure.[89] X-ray crystallographic analysis indicated the absence of σ-dimer and π-dimer (Fig. 18a and b), and instead, only C–H···π interactions could be observed. Even though, a room-temperature conductivity of 0.05 S cm^{-1} could be achieved. As shown in Fig. 18c, it was speculated that the delocalized

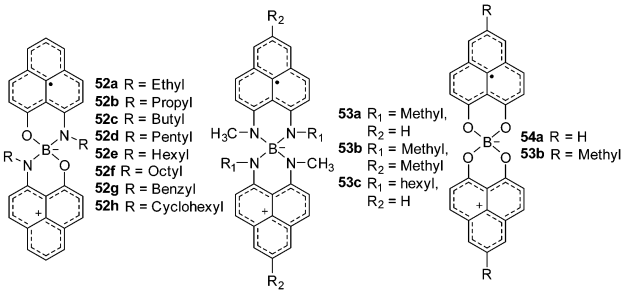

Fig. 17 Spiro-bisphenalenyl boron radicals.

electronic conduction band (0.5 eV) should be responsible for the transport properties of **52e**. However, it was separated from the ground state of **52e**, or a degenerate Mott–Hubbard insulator, by an energy gap corresponding to the on-site Coulomb repulsion energy (U = 0.4 eV), which allowed the thermal population of electrons to conduction bands possible.

Later, by adjusting hexyl groups to ethyl and butyl ones, compound **52a** and **52c** were synthesized, with the change from C–H···π interactions to π-dimers as observed in the crystal structures (Fig. 18d).[90] Interestingly, **52a** and **52c** exhibited bistability in electrical, optical and magnetic aspects. For example, the distance of the π-dimer was about 3.3 Å at a high temperature ($T > 350$ K); however, when T decreased below 320 K, the distance shortened to about 3.2 Å. As shown in Fig. 18e, at high temperatures, the two radicals were located in the two outer phenalenyl moieties of the π-dimer with paramagnetic properties, whereas at low temperatures, the two radicals moved to the inner phenalenyl units and behaved as π-dimers with a diamagnetic character. Correspondingly, the conductivity sharply increased by two orders of magnitude in the diamagnetic state.[91]

By further changing the substituents to cyclohexyl groups, **52h** showed a spiro-conjugated 2D-like structure with effective π–π overlaps of neighbour molecules (Fig. 19). Therefore, the room-temperature conductivity was 0.3 S cm^{-1}, which could be ascribed to the quarter-filled energy band and the significant reduction of on-site Coulomb repulsion energy band U.[92] However, the introduction of more alkyl chains was harmful for charge transport. For example, by changing two O atoms to methylamine groups, the conductivity decreased to 4×10^{-2} and 1×10^{-2} S cm^{-1} for **53a** and **53b**, respectively.[93] The attempt by reducing the substituents of changing alkylamine groups to O atoms produced **54a** and **54b**. Single crystal analysis revealed their continuous array of π–π stacking structures with very short intermolecular C–C contacts. Thus, **54a** and **54b** exhibited the conductivities of 0.1 and 0.3 S cm^{-1}, respectively.[93]

4,8,12-Trioxotriangulene (Fig. 20a) radicals represented another kind of stable monoradical even without steric protection due to the delocalization of spin density on the whole backbone with 25π electrons (Fig. 20b).[94] Similar to phenalenyl radicals, X-ray crystallographic analysis of **55a** revealed the formation of a π-dimer with a shortest C–C distance of 2.987 Å, much shorter than the sum of van der Vaals radii of two sp^2 carbons (3.40 Å).[95] The dimers stacked together to construct a 1D column with a much larger intradimer distance of 3.684 Å (Fig. 20c).

By introducing different substituents, **55b–f** showed a similar 1D column but with different intradimer distances.[96] Therefore, DFT calculations revealed their different intermolecular overlap integrals of singly occupied molecular orbital (SOMO) of intra- and inter-dimers, for example, **55b** showed about 15 times larger intermolecular overlap integrals (s_1) than that of interdimer one (s_2). However, **55f** formed a uniform 1D slipped π-stacking column with a π–π distance of 3.43 Å, and the overlap integral was around 2×10^{-3}. As mentioned above, the conduction barrier in the 1D array was defined as U-4β, and obviously, a strong orbital

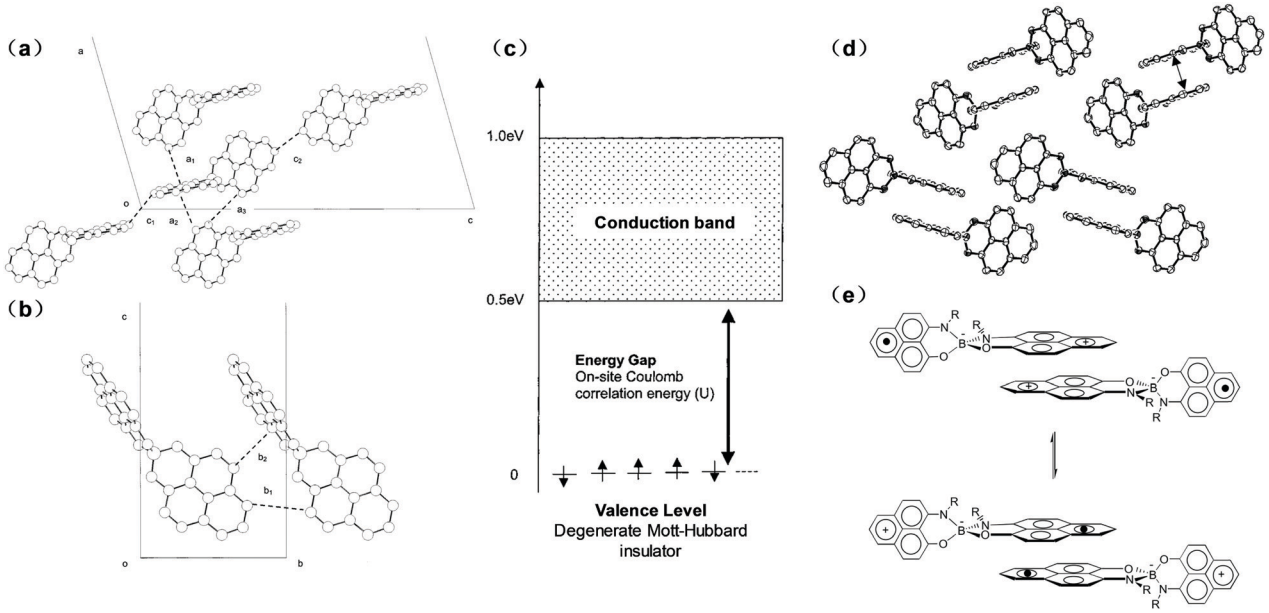

Fig. 18 (a and b) Closest intermolecular contacts between the phenalenyl units in the crystal structure of **52e**. (c) Proposed electronic structure of crystalline **52e**. (d) X-ray crystal structure of ethyl radical **52a** with a π-dimer. (e) Interconversion between the diamagnetic π-dimer (bottom: low temperature form) and the paramagnetic π-dimer (top: high-temperature form) of **52a**. Adapted with permission from ref. 89, American Chemical Society (a–c), ref. 91, AAAS.

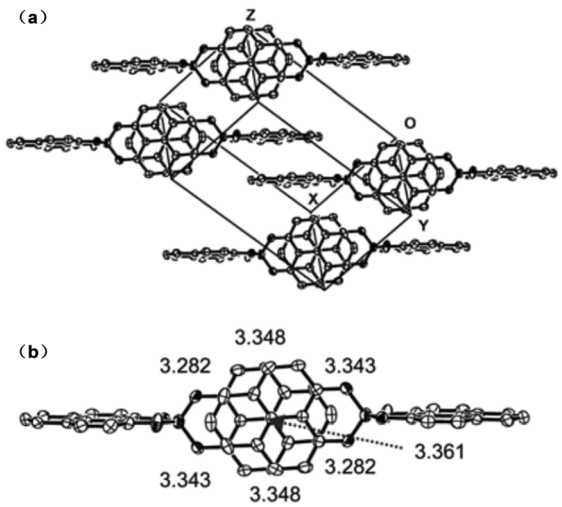

Fig. 19 (a) Unit cell of the X-ray crystallographic structure of **52h** viewed normal to one of the phenalenyl planes, (b) π–π overlaps and C–C distances (in Å) between the π-dimers of **52h**. Copyright 2005, AAAS.

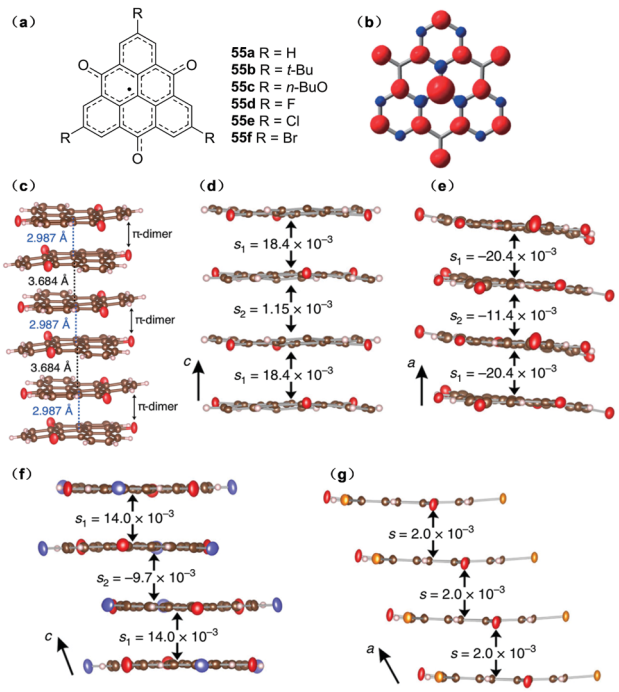

Fig. 20 (a) 4,8,12-Trioxotriangulene radical structure, (b) DFT calculated (the UBLYP/6-31G** level) electronic spin density distribution, and their X-ray crystallographic structure with 1D π-stacked radical columns of (c) **55a**, (d) **55b**, (e) **55c**, (f) **55d** and (g) **55f** and intermolecular overlap integrals. Adapted with permission from ref. 96, Springer Nature.

overlap was essential for the generation of high conductivity. The different inerdimer and intradimer interactions in turn resulted in the corresponding electron conductivities of 10^{-8}, 1.2×10^{-3}, 8.1×10^{-5} and 1.8×10^{-3} S cm^{-1} for **55b**, **55c**, **55d** and **55f**, respectively.

In principle, high pressure would compress the crystallographic lattice and increase the intermolecular overlap integrals, which in consequence, probably generate monoradical conductors. In 2016, Veciana *et al.* reported a TTF linked polychlorotriphenylmethyl radical **56**.[96] In the crystallographic structure (Fig. 21a), **56** formed a 1D herringbone structure with head-to-tail TTF units packing together and a S–S distance of 3.9 Å, which provided a possible charge transport channel.

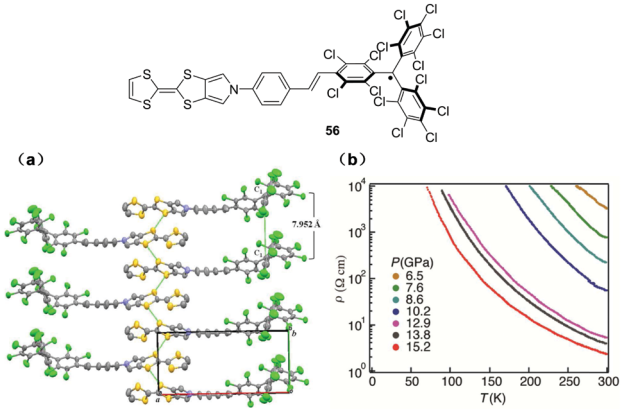

Fig. 21 Chemical structure of **56**, its (a) crystal packing of **56** on the *ab*, and (b) temperature dependence of the resistivity of **56**. Adapted with permission from ref. 97, American Chemical Society.

Pressure and temperature dependence measurements (Fig. 21b) showed that **56** exhibited insulator characteristics under ambient pressure and room temperature, while the conductivity of **56** at 15.2 GPa and 298 K was 0.76 S cm^{-1}. For comparison, polychlorotriphenylmethyl radical **4a** always showed insulator properties even at 21.2 GPa. DFT calculations revealed that upon increasing the pressure, the electronic bandwidth (W) of **56** increaseed, and once it is larger than the coulomb repulsion (U), the change from insulator to conductor would happen.

5. Aggregated open-shell organic luminescent materials

Organic luminescent materials have already brought revolutionary progress to our daily life, for example, OLED-based display screens are gradually replacing traditional liquid-crystal screens due to their superior characteristics such as flexibility, light weight, brighter colour, and so on.

Open-shell diradicaloids usually show no fluorescence, which is the typical character of singlet diradicaloids. Monoradicals or triplet diradicaloids have spin-allowed fluorescence transition from their doublet or triplet lowest excited state to the corresponding doublet or triplet ground state. Different from conventional closed-shell fluorescent compounds with only 25% internal quantum efficiency due to annihilation according to spin statistics, monoradicals or triplet diradicaloids can emit 100% theoretically.[22] However, the progress in this area is largely confined due to the low fluorescence quantum yield of monoradicals or triplet diradicaloids. For example, **4b** only showed a fluorescence quantum yield of 0.03 with a maximum of 563 nm in cyclohexane. Early in 2006, Juliá *et al.* synthesized monoradical **57a** (Fig. 22) by linking **4b** and carbazole together. Interestingly, **57a** showed much red-shifted fluorescence emission with a maximum of 628 nm and an enhanced fluorescence quantum yield of 0.53 in cyclohexane compared to that of **4b**, which was almost 18 times higher than that of **4b**.[98] Interestingly, **4b** showed strong solvent-dependence fluorescence phenomena with obvious red-shifted Stokes shift

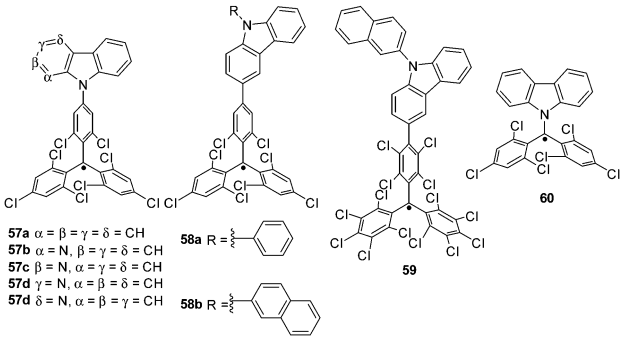

Fig. 22 Chemical structures of multi-chlorinated organic monoradical derivatives.

values from nonpolar cyclohexane to polar chloroform solvent, indicating its high dipole moment in the excited state. It is worth noting that although the absorbance coefficient of the maximum of **57a** (3740 $Lmol^{-1}$ cm^{-1} at 597 nm) is higher than that of **4b** (840 L mol^{-1} cm^{-1} at 542 nm), it still remained at a relatively low level. Therefore, how to improve the absorbance coefficient of these monoradicals is a critical factor to realize high-efficiency OLEDs.

Furthermore, the OLED performance of **57a** (Fig. 22) has never been reported, probably due to its aggregation-caused quenching behaviour in the thin-film state. Excitedly, Li *et al.*, for the first time, fabricated OLED devices of **57a** by doping the monoradical into a matrix of 4,4′-bis(carbazol-9-yl)biphenyl. The optimized maximum external quantum efficiency (EQE) (η_{EQE}) of **4b** was up to 2.4% with electroluminescence at 692 nm.[99] Later, by introducing 3-phenyl-9*H*-carbazole and 3-substituted-9-(naphthalene-2-yl)-9*H*-carbazole into **4b**, **58a** and **58b** were prepared, and the performance of OLEDs could be improved to 17% and 27% with a deep-red emission at 703 nm and 710 nm, respectively.[100] The high luminescence efficiency could be ascribed to the charge-transfer state, which could break the alternative symmetry of molecular structures and lift the degeneracy of the lowest energy orbital excitations. By further finely tuning the N position of pyridoindolyl groups, Li *et al.* also synthesized **57b–d**, and the photoluminescence quantum yields could be as high as 91%, 89%, 32% and 99% with pure-red emissions at 620 nm, 635 nm, 612 nm and 643 nm, respectively. Finally, highly efficient OLEDs with the maximum EQE of 9.6%, 12.2%, 2.9% and 9.5% for **57b–d**, respectively, could be realized. Compared to the relative low performance of **57a** in OLED devices, **57b–d** are much better doublet emitters. This could be ascribed to the non-alternant structures of these pyridine containing **57b–d**, which would lift of the degeneracy of the lowest energy orbital excitations and the intensity borrowing from an intense high-lying transition by the low energy excitation could enhance the oscillator strength of these monoradicals.[101]

Recently, they reported that compound **59** (Fig. 22) violated the Aufbau principle with its SOMO lying below the HOMO and HOMO-1 (Fig. 23), and the special electronic structure would reduce the chemical activity of the single occupied electron and enhance the stability of the monoradical. Therefore, the half-

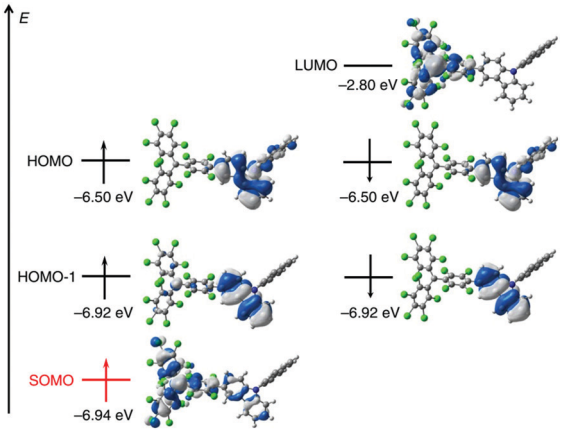

Fig. 23 Energies and wavefunctions for the frontier molecular orbitals of **59**. Adapted with permission from ref. 102, Springer Nature.

lives could reach up to several months even under UV light radiation. Furthermore, OLED-based **59** showed a deep-red emission (700 nm) with a maximal EQE of 5.3%.[102]

Li *et al.* also synthesized a new luminescent biphenylmethyl radical **60** (Fig. 22) with N atoms in the carbazole ring directly linked to the carbon radical centre.[103] EPR spectroscopy results (Fig. 24b) confirmed the existence of the unpaired electron with g = 2.0035. X-ray single crystal analysis showed that (Fig. 24a) radicals C13, N1, C14, and C20 lied in the same plane. The molecule was propeller shaped, and the adjacent molecules were linked together by multiple C–H···π hydrogen bonds. The

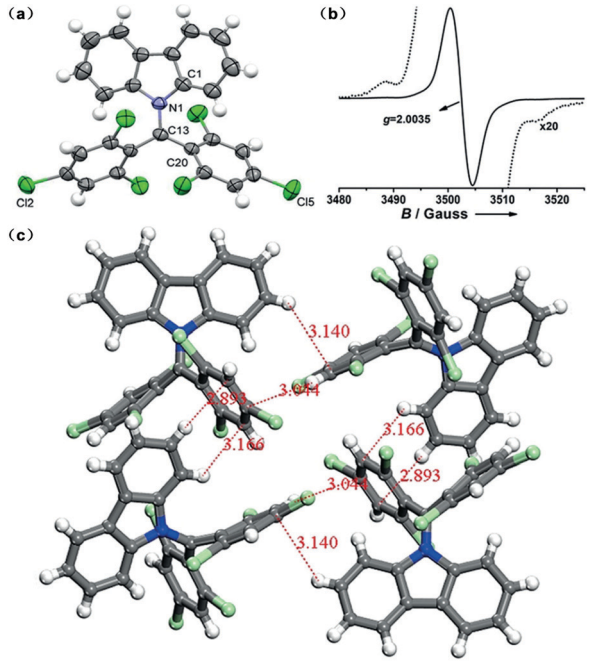

Fig. 24 (a) Crystal structure of **60** with thermal ellipsoids set at 50% probability. (b) Experimental EPR spectra (line) of **60** in cyclohexane at room temperature. Enlarged portion of the spectra (20 fold; dotted line) shows the hyperfine coupling of ^{13}C(α). (c) Multiple C–H···π hydrogen bonds in **60** crystals. Copyright 2018, Wiley-VCH Verlag GmbH & Co.

60 in cyclohexane solution emited at 697 nm with an absolute fluorescence quantum yield (PLQY) of 2.0%. And, OLED devices showed its maximal EQE of 0.66%.

For open-shell species, especially monoradicals, the degradation problem under photoexcitation has always been a hindrance for the development of this area. In 2014, Nishihara *et al.* reported (3,5-dichloro-4-pyridyl)-bis(2,4,6-trichlorophenyl) methyl radical **5a** (Fig. 3) with fluorescence quantum yields of 0.03, 0.26, and 0.81 in solution, in a PMMA film at room temperature and in an EPA matrix (diethyl ether:isopentane: ethanol) at 77 K, respectively.[34] Furthermore, the photostability of **5a** was 115 times higher than that of **4b**, which could be ascribed to the introduction of the pyridyl group with the lowered energies of molecular orbitals. Later, by changing the halogen atoms on pyridyl from Cl atoms to Br and F atoms, Nishihara *et al.* synthesized **61a** and **61b** (Fig. 25). It was found that the halogen atoms did not affect the SOMO strongly, whereas the electronegativity of halogens showed obvious effects on their HOMOs. Therefore, as shown in Fig. 26, the absorption and emission of the three compounds exhibited bathochromically in the order of F < Cl < Br.[104]

Based on pyridine chemistry, Nishihara *et al.* further developed a series of luminescent open-shell radicals. By coordinating **5a** with Au^{I}, they synthesized **62a** and **62b** (Fig. 25).[105] The Au^{I} complex of **62b** exhibited bathochromically shifted fluorescence with a maximum peak at 653 nm compared to that of **4b** (λ_{em} = 585 nm), which could be ascribed to the excitation of the transition band from the D_1 state to the D_0 state on the pyridyl radical centre. Another example by methylating and coordinating $B(C_6F_5)_3$ to the pyridyl imine N atom, Nishihara *et al.* synthesized **63** and **64** (Fig. 25).[106] Further studies indicated that the chemical modification on imine N atoms showed great influence on the β-SOMO, which determined the optical and electrochemical properties. Therefore, compared to that of **5a**, **63** and **64** showed red-shifted emission to the low-energy region with maximum wavelengths of 712 nm and 660 nm, respectively. They also reported Cu^{II} and Zn^{II} complexes with two pyridyl radicals **5a** as

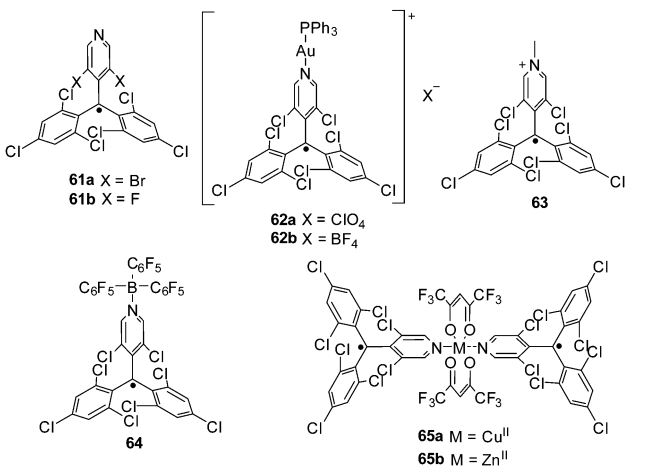

Fig. 25 Chemical structures of multi-chlorinated pyridyl organic monoradical derivatives.

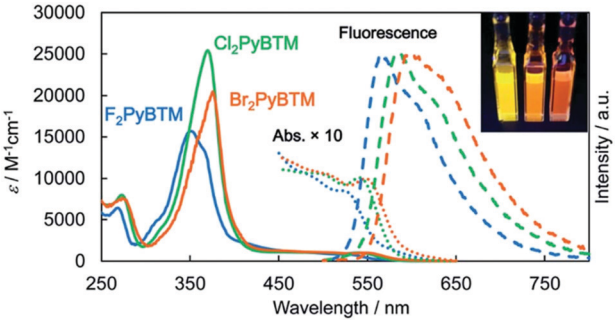

Fig. 26 Absorption (solid lines) and corrected emission spectra (dashed lines) of **61a** (orange), **5a** (green), and **61b** (blue) in CH_2Cl_2. Copyright, The Royal Society of Chemistry 2015.

ligands, and both **65a** and **65b** showed a hexacoordinated structure with an elongated octahedral geometry.[107] However, the longer Zn–N bond length compared to the Cu–N bond length resulted in the axially coordinated Zn^{II} complex and equatorially coordinated Cu^{II} complex. Magnetic studies indicated that **65a** displayed an efficient intramolecular ferromagnetic exchange interaction between the two radical centres and Cu^{II} based on the orthogonality of the two spin orbitals.

In 2019, Nishihara *et al.* reported a 1D magnetic chain **66a** (Fig. 27) consisting of Cu^{II} and polychlorinated dipyridylphenylmethyl radical **5b**.[108] As shown in Fig. 27, a 1D –Cu^{II}(hfac)$_2$–**5b**– type zigzag chain structure formed along the $a + c$ direction, and these 1D chains stacked together to form a layered structure. The temperature-dependent Jahn–Teller (JT) distortion was observed due to the Jahn–Teller axis rotation from the Cu–N bond direction at 298 K to the Cu–O bond direction at 93 K. Therefore, the intramolecular ferromagnetic interaction was enhanced by the reorientation of the Cu^{II} $d_{x^2-y^2}$ orbital at low temperatures caused by the JT distortion.

Very recently, Nishihara *et al.* reported the preparation of tris(3,5-dichloro-4-pyridyl)methyl radical **5c**, which exhibited much better photostability with a half-life of 2.2×10^4 s. And, the half-life of mono-pyridyl **5a**, di-pyridyl **5b** and tri-pyridyl **5c** is 4, 160, 10 000 and times that of TTM **4b**, respectively, which was beneficial for the introduction of more imine N atoms and gradually decreased the energy levels of frontier orbitals.[36] Therefore, from **4b**, **5a**, and **5b** to **5c**, the maximal emission peak in solution was steadily red-shifted like the increased number of imine N atoms on the TTM skeleton with the values of 570, 585, 650 and 700 nm, respectively. In the solid state, **5c** showed a blue-shifted emission peak at 665 nm. Complexation of **5c** and Zn^{II}(hfac)$_2$ afforded 2D coordination polymers **67**. As shown in Fig. 27c, **67** processed honeycomb spin-lattices with a graphene-like spin topology and exhibited luminescence at 79 K with a maximal emission peak of 695 nm, which was a rarely observed open-shell 2D structure with luminescence characteristics. Magnetic property measurements further confirmed the existence of one unpaired racial electron on each **5c** unit without the loss of its radical character upon the formation of 2D polymer **67**.

Nishihara *et al.* further reported the luminescence properties of monoradicals **5b** and **5c**, together with the 1D chain **66b**

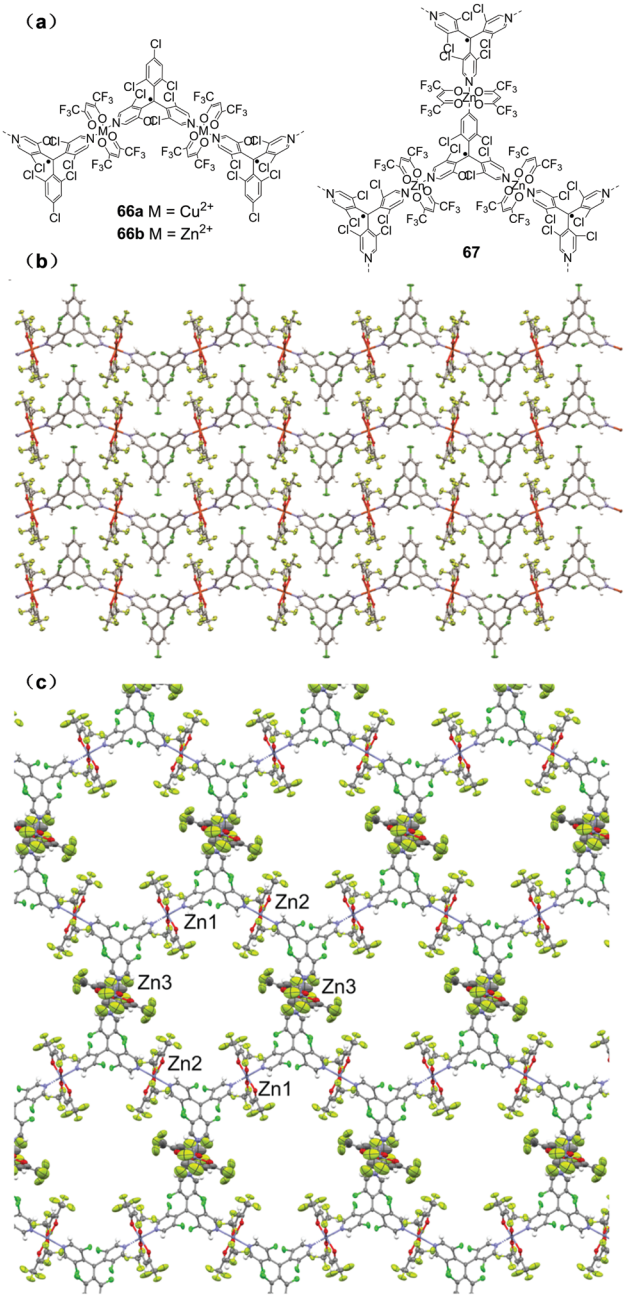

Fig. 27 (a) Chemical structures of 1D and 2D magnetic molecules, X-ray crystal structure of (b) **66a** and (c) **67**. Adapted with permission from ref. 108, The Royal Society of Chemistry (a), ref. 36, American Chemical Society.

and 2D network **67** under a magnetic field upon temperature changes.[36] As shown in Fig. 28a and b, the emission spectra of **5b** and **5c** were almost unaffected by the external magnetic field. In contrast, the emission spectra of coordination polymers **66b** and **67** showed significant magnetic field-dependent characters. The 1D coordination polymer **66b** had almost no emission at 4.2 K and 0 T, upon increasing the applied magnetic field, emission peaks at 626 and 675 nm gradually appeared (Fig. 28c). And, the emission intensity of **67** increased by 25% when the magnetic field reached 18 T. This phenomenon could

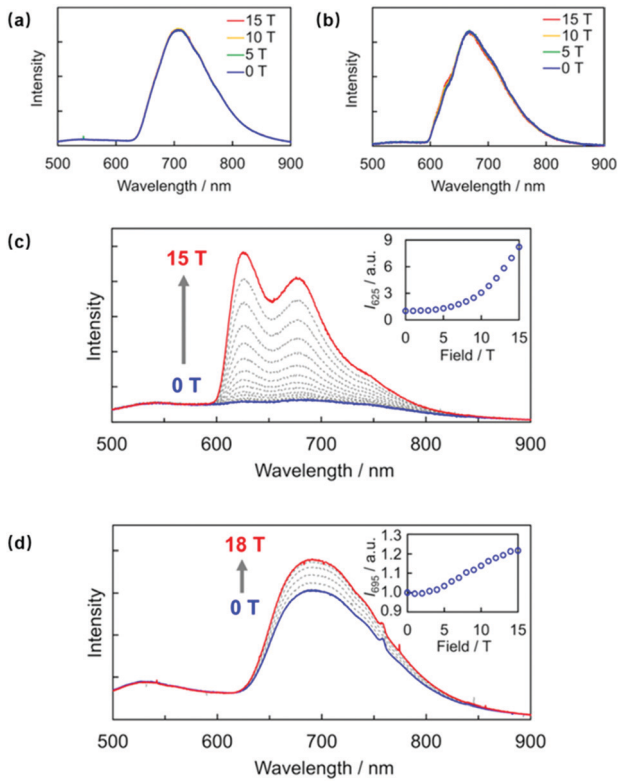

Fig. 28 Emission spectra of (a) **5b**, (b) **5c**, (c) **66b**, and (d) **67** at 4.2 K under a magnetic field. Insets in (c and d) indicate the magnetic-field dependencies of emission intensities at 4.2 K of **66b** and 67 at λ_{em} = 625 and 695 nm, respectively. Adapted with permission from ref. 109 American Chemical Society.

be explained by the modulation of radical–radical ground-state interactions, and the reduction of radical–radical interactions in coordination polymers by Zn^{II} would be the key point for the magnetoluminescence phenomena.

6. Aggregated organic photoinduced radical materials

Except for pure monoradicals, photoinduced organic radicals were found to be pivotal for the emission process of triphenylamine or triphenylphosphine-based close-shell materials upon light exposure. Recently, their possible mechanism and potential applications were preliminarily studied.

Giuseppone *et al.* found that tryarylamine derivatives were photoactive materials, which could generate radicals upon even white light irradiation. For example, compounds **68** and **69** (Fig. 29) in chloroform solution could form a proportion of triaryammonium cationic radical of up to 44% as a function of irradiation time with a halogen lamp.[110,111] Further study indicated that the self-assembly nanostructure of **69** could display healable supramolecular properties and metallic behaviour. However, its emission phenomena have not been mentioned.[111]

As shown in Fig. 30, Chi *et al.* reported **70** (Fig. 29) to be a photoinduced radical material, which unexpectedly exhibited a

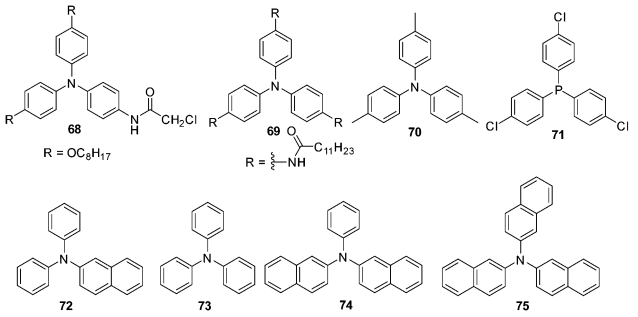

Fig. 29 Chemical structures of **68–75**.

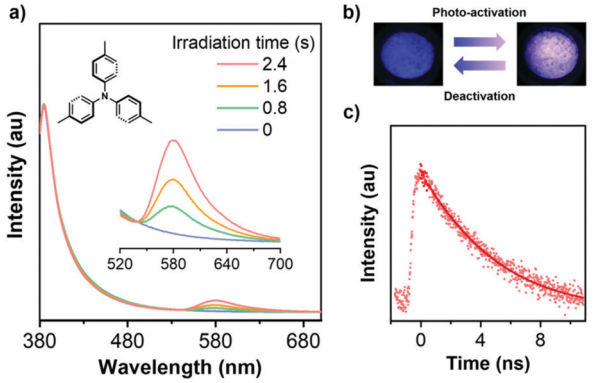

Fig. 30 (a) Photoluminescence spectra of **70** crystal under UV light irradiation with different irradiation times: 0, 0.8, 1.6, and 2.4 s, respectively. (b) Photographs of **70** crystal taken under UV lamp irradiation without (left) and under (right) continuous irradiation. (c) Luminescence intensity decay curve of **70** crystal at the 580 nm peak after it irradiated for 5 s. Copyright 2021, Wiley-VCH Verlag GmbH & Co.

rapid and reversible luminescent colour change from blue to pinkish-purple in the single-crystal state by light irradiation under ambient conditions.[112] An emission peak appeared at around 580 nm upon UV light irradiation, while the intensity significantly enhanced in response to the prolonged irradiative time. However, the phenomena could not be observed in the amorphous phase, indicating the importance of intermolecular interactions. The lifetime of this new peak at 580 nm was also measured to be 4.2 ns, revealing its fluorescence property (Fig. 30c). X-ray crystallographic analysis revealed the absence of π–π interactions, and C–H···π interactions in the crystalline sate well separated the photoinduced radical cation molecules from each other, which is beneficial for the effective rapid release of its energy from the excited state to the ground state. Furthermore, this molecule could be integrated to a dual-channel photosensitive device, and showed luminescence and conducting switching upon UV light irradiation.

Recently, Tang *et al.* reported the photoinduced generation of radicals with bright red emission (Fig. 31a), which could be ascribed to the formation of a radical cation in crystalline **71**.[113] As shown in Fig. 31b, after irradiation, **71** (***i*-71**) showed two new absorption peaks around 496 and 520 nm. ESR measurements (Fig. 31c) demonstrated the existence of radical species in the

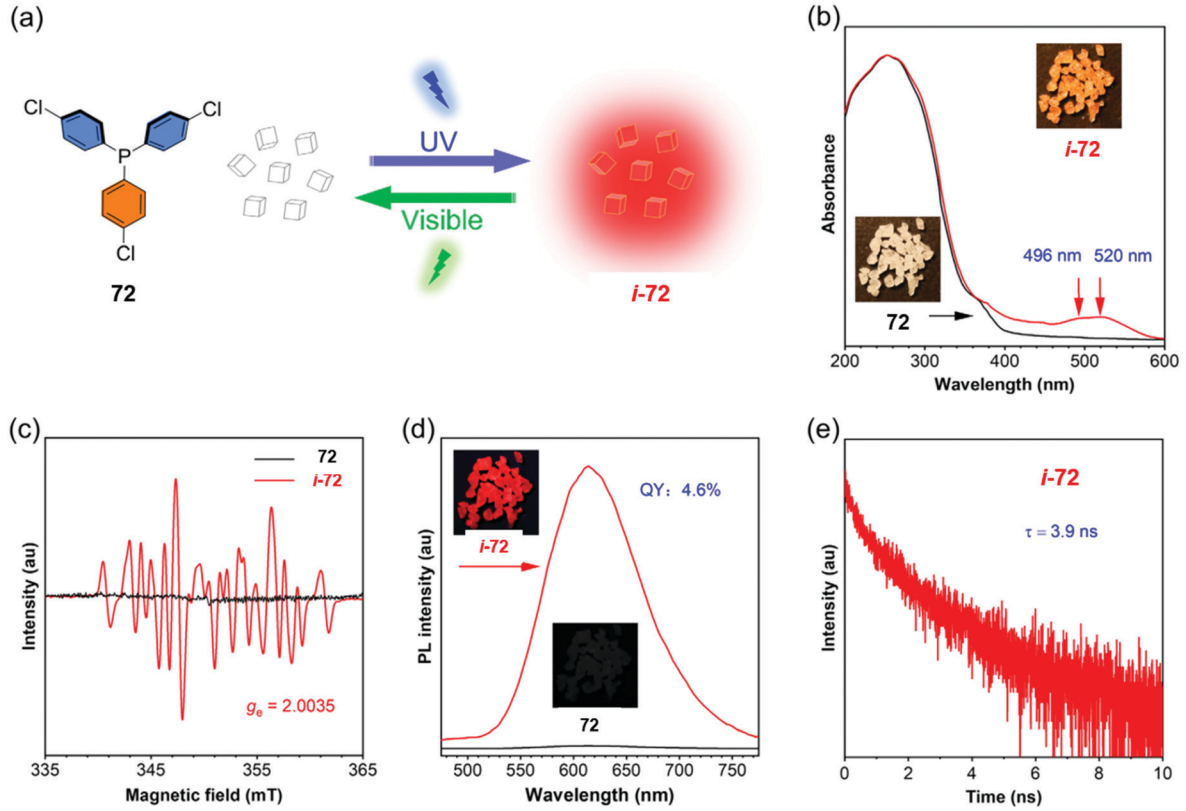

Fig. 31 (a) Schematic diagram of the photoinduced radical generation process. (b) UV–vis spectra, (c) EPR spectra, and (d) PL spectra of **71** crystals before and after UV light exposure for seconds at room temperature, λ_{ex} = 365 nm. The insets in (b) and (d) show the photographs of colour and emission changes, QY = quantum yield. (e) Time-resolved PL decay curves of ***i*-71** measured at λ_{max} = 620 nm at room temperature, λ_{ex} = 400 nm. Adapted with permission from ref. 113, Chinese Chemical Society publishing.

crystal core. The PL emission lifetime of ***i*-71** with a value of 3.9 ns (Fig. 31d) revealed the fluorescence character of the emission. Similar to that of **70**, the emission disappeared after grinding, indicating the importance of crystal lattice acting as a protective cage to isolate **71** from water and ambient oxygen. Notably, the radical **71** and its red emission could survive for more than seven days in the crystalline state in air. DFT calculations and single-crystal analysis further revealed the unique symmetry breaking phenomena in single crystals of **71**, which in turn caused the molecular conformation change and photoredox characteristic change. In a single crystal, the asymmetric conformation with an intermolecular π–π distance of 3.29 Å arrangement may promote the exciton separation and stabilization according to the charge hopping mechanism. The study here provided a possible way to generate *in situ* stable radicals upon visible light irradiation as photosensitive materials.

Very recently, our group's work revealed the importance of cationic radicals in the photoresponsive process of a series of triarylamine compounds from **72** to **75** (Fig. 29).[114] As shown in Fig. 32, by dispersing these triarylamine compounds into a poly(methylmethacrylate) (PMMA) matrix, **72**@PMMA films showed the photoactivated phosphorescence phenomena, while **73**@PMMA demonstrated only fluorescence without phosphorescence characteristics. In detail, **72**@PMMA exhibited irradiation time-dependent room-temperature phosphorescence (RTP) intensity, quantum yield and lifetime, which could be ascribed to the triplet oxygen consumption after long-time UV irradiation. However, **74** and **75** had no RTP phenomena but

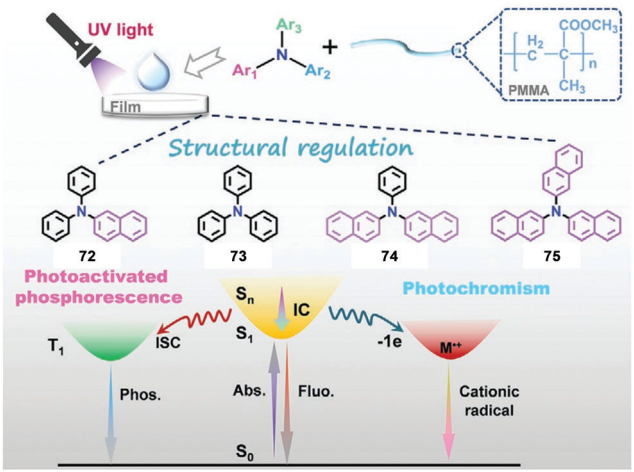

Fig. 32 Schematic representation of the structure of triarylamine derivatives **72** to **75** and the photoactivated phosphorescence and photochromic properties in the PMMA film. Copyright 2021, Wiley-VCH Verlag GmbH & Co.

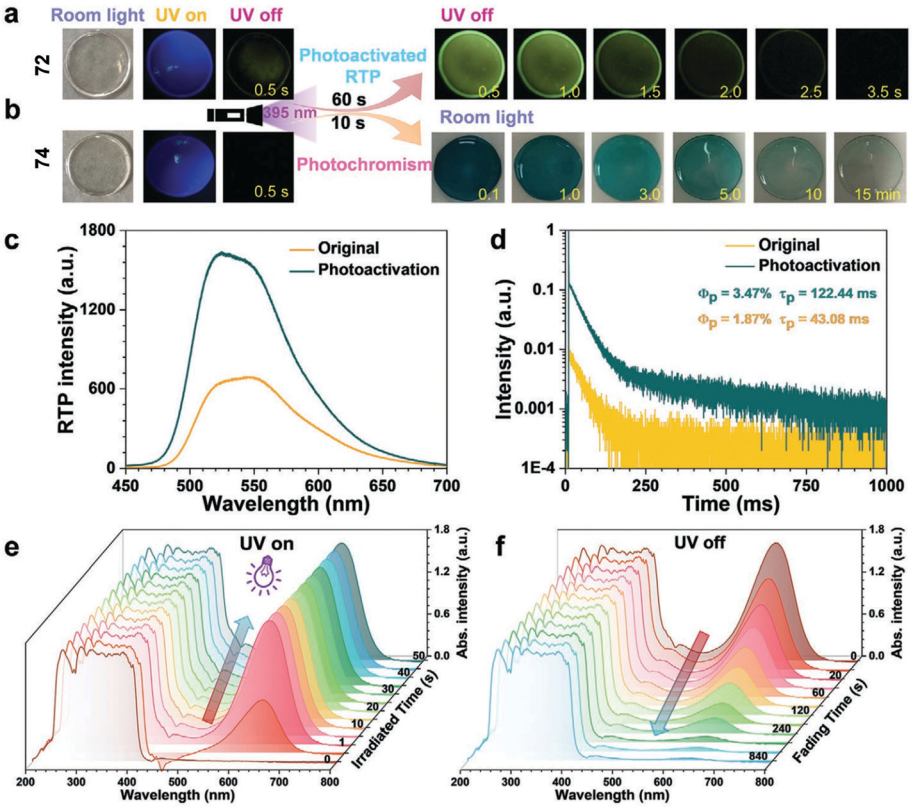

Fig. 33 Photophysical properties of the photoresponsive system under ambient conditions. (a) The room-temperature phosphorescence (RTP) behavior of the 72@PMMA film under the 395 nm UV irradiation. (b) The photochromic behaviour and fading process of the 74@PMMA film at room temperature. The photographs were taken at different times before and after turning off the 395 nm UV light under ambient conditions. (c) The room-temperature phosphorescence spectra of the 72@PMMA film before and after the 395 nm UV irradiation for 1 min. (d) Time-resolved PL-decay curves for the room-temperature phosphorescence of the 72@PMMA film before and after the 395 nm UV irradiation for 1 min. (e) Time-dependent UV spectra of the 74@PMMA film under the 395 nm UV irradiation for 50 s. (f) Time-dependent UV spectra for the fading process of the 74@PMMA film. Copyright 2021, Wiley-VCH Verlag GmbH & Co.

significant change in absorption (Fig. 33b). Taking **74** for example, as shown in Fig. 33e, the **74**@PMMA film showed a maximum photochromic effect upon irradiation for 30 s, and faded from green to colourless after about 15 minutes. This process could be ascribed to the formation of cationic radicals under UV light irradiation, and ESR analysis further demonstrated the existence of open-shell species through photoinduced electron transfer. Interestingly, this process could be repeated for more than 20 times. Therefore, based on these controllable phosphorescence and photochromic phenomena, information encryption and decryption, anticounterfeiting and rewritable information recording have been successfully realized.

7. Summary and perspectives

Based on traditional thoughts, open-shell organic π-conjugated compounds are considered to be unstable species, which may limit their possible applications. Actually, the combined optical, electrical and magnetic characteristics of organic open-shell materials are quite appealing in the material world. In the last few decades, the stability problem of open-shell materials has dramatically changed due to the developed novel strategies, which are universally effective towards air-stable open-shell compounds, such as kinetically steric protection, spin density delocalization and heteroatom-assisted protection. Therefore, scientists could expand their attention towards the possible applications of open-shell magnetic materials. Consequently, we summarized the recent applications of open-shell organic conjugated materials in OFETs, one-component organic conductors, luminescent areas and photosensitive devices, mainly focusing on the general progress of novel developed organic open-shell magnetic materials and the effect of solid-state aggregation on their basic electrical and optochemical characteristics.

Although great progress has been made in both open-shell material design and the exploration of their novel applications in the past, there are still quite a number of scientific problems to be further tackled. Accordingly, future research perhaps should focus on these issues:

(1) The intrinsic charge transport difference between common closed-shell semiconductors and open-shell organic materials is still not clear. For example, the self-doping behaviour

of organic semiconductors with open-shell diradical ground states is an emerging hot topic in this area. Theoretically, by reducing the temperature to a certain degree, open-shell diradicaloids should also behave as pure semiconductors rather than intrinsic conductors due to the lack of thermally activated charge carriers. Several examples of diradicaloids with remarkable conductivities reported up to now are limited to compounds with narrow band gaps and low-lying LUMO energy levels. However, their temperature-dependent measurements are rarely investigated.

(2) One of the important research areas of organic open-shell materials is how to design molecules with both electrical and magnetic response characteristics, like spintronic devices. However, rare examples have been reported so far.

(3) For one-component organic monoradical conductors, the main problem is the lack of new monoradicals with good stability and ease of chemical modification. Therefore, the development of novel monoradicals is always the hot topic of this area, while another challenge is how to overcome the on-site neighbour Coulomb repulsion by delicate material design or special processing techniques.

(4) For open-shell luminescent materials, the main problem is how to improve their fluorescence quantum efficiency; in other words, the low fluorescence quantum efficiencies of radical species limit the progress of this area. On the other hand, open-shell luminescent materials now available are limited to monoradial species, and the expansion of open-shell luminescent materials towards triplet diradicals or even materials with high spin states still remain quite challenging.

(5) For photosensitive materials, photoinduced radical species are important for luminescence and photochromic phenomena. However, the intrinsic mechanism remains to be further explored. Besides, seeking for more photosensitive materials is also an attracting topic.

Conflicts of interest

There are no conflicts to declare.

Acknowledgements

This work was financially supported by the starting grants of Tianjin University and Tianjin government.

Notes and references

1 Q. Li and Z. Li, *Acc. Chem. Res.*, 2020, **53**, 962–973.
2 Y. Wang, J. Yang, M. Fang, Y. Yu, B. Zou, L. Wang, Y. Tian, J. Cheng, B. Z. Tang and Z. Li, *Matter*, 2020, **2**, 449–463.
3 R.-L. Tang, S.-M. Zhou, Z.-Y. Cheng, H. Chen, L. Deng, Q. Peng and Z. Li, *CCS Chem.*, 2020, **2**, 1040–1048.
4 F. Liu, S. Bi, X. Wang, X. Leng, M. Han, B. Xue, Q. Li, H. Zhou and Z. Li, *Sci. China: Chem.*, 2019, **62**, 739–745.
5 J. Yang, Z. Chi, W. Zhu, B. Z. Tang and Z. Li, *Sci. China: Chem.*, 2019, **62**, 1090–1098.
6 A. Rajca, *Chem. Rev.*, 1994, **94**, 871–893.
7 B. Zhang and D. Zhu, *Sci. China: Chem.*, 2012, **47**, 883–892.
8 M. Abe, *Chem. Rev.*, 2013, **113**, 7011–7088.
9 M. Winkler and W. Sander, *Acc. Chem. Res.*, 2014, **50**, 31–44.
10 Z. Zeng, X. Shi, C. Chi, J. T. L. Navarrete, J. Casado and J. Wu, *Chem. Soc. Rev.*, 2015, **44**, 6578–6596.
11 T. Kubo, *Chem. Lett.*, 2015, **44**, 111–122.
12 C. K. Frederickson, B. D. Rose and M. M. Haley, *Acc. Chem. Res.*, 2017, **50**, 977–987.
13 X. Shi and C. Chi, *Top. Curr. Chem.*, 2017, **375**, 68.
14 A. Konishi and T. Kubo, *Top. Curr. Chem.*, 2017, **375**, 83.
15 P. M. Burrezo, J. L. Zafra, J. T. L. Navarrete and J. Casado, *Angew. Chem., Int. Ed.*, 2017, **56**, 2250–2259.
16 T. Y. Gopalakrishna, W. Zeng, X. Lu and J. Wu, *Chem. Commun.*, 2018, **54**, 2186–2199.
17 X. Hu, W. Wang, D. Wang and Y. Zheng, *J. Mater. Chem. C*, 2018, **6**, 11232–11242.
18 K. Kato and A. Osuka, *Angew. Chem., Int. Ed.*, 2019, **58**, 8978–8986.
19 S. Dong, A. Ong and C. Chi, *J. Photochem. Photobiol., C*, 2019, **38**, 27–46.
20 L. Ji, J. Shi, J. Wei, T. Yu and W. Huang, *Adv. Mater.*, 2020, 1908015.
21 Y. Teki, *Chem. – Eur. J.*, 2020, **26**, 980–996.
22 Z. Cui, A. Abdurahman, X. Ai and F. Li, *CCS Chem.*, 2020, **2**, 1129–1145.
23 Z. Chen, Y. Li and F. Huang, *Chem*, 2021, **7**, 1–45.
24 D. Yuan, W. Liu and X. Zhu, *Chem*, 2021, **7**, 333–357.
25 W. Zeng and J. Wu, *Chem*, 2021, **7**, 358–386.
26 M. Slota, A. Keerthi, W. K. Myers, E. Ttretyakov, M. Baumgarten, A. Ardavan, H. Sadeghi, C. J. Lambert, A. Narita, K. Müllen and L. Bogani, *Nature*, 2018, **557**, 691–696.
27 R. Kuhn, F. A. Neugebauer and H. Trischmann, *Angew. Chem., Int. Ed. Engl.*, 1965, **4**, 72.
28 J. Fujita, M. Tanaka, H. Suemune, N. Koga, K. Matsuda and H. Iwamura, *J. Am. Chem. Soc.*, 1996, **118**, 9347–9351.
29 L. Balents, *Nature*, 2010, **464**, 199–208.
30 Y. Wu, M. D. Krzyaniak, J. F. Stoddart and M. R. Wasielewski, *J. Am. Chem. Soc.*, 2017, **139**, 2948–2951.
31 M. Gomberg, *J. Am. Chem. Soc.*, 1900, **22**, 757–771.
32 S. H. Jang, P. Gopalan, J. E. Jackson and B. Kahr, *Angew. Chem., Int. Ed. Engl.*, 1994, **33**, 775–777.
33 M. Ballester, *Acc. Chem. Res.*, 1985, **18**, 380–387.
34 Y. Hattori, T. Kusamoto and H. Nishihara, *Angew. Chem., Int. Ed.*, 2014, **53**, 11845–11848.
35 S. Kimura, A. Tanushi, T. Kusamoto, S. Kochi, T. Satobc and H. Nishihara, *Chem. Sci.*, 2018, **9**, 1996–2007.
36 S. Kimura, M. Uejima, W. Ota, T. Sato, S. Kusaka, R. Matsuda, H. Nishihara and T. Kusamoto, *J. Am. Chem. Soc.*, 2021, **143**, 4329–4338.
37 T. Nishiuchi, S. Aibara and T. Kubo, *Angew. Chem., Int. Ed.*, 2018, **57**, 16516–16519.
38 J. Thiele and H. Balhorn, *Chem. Ber.*, 1904, **37**, 1463–1470.
39 L. K. Montgomery, J. C. Huffman, E. A. Jurczak and M. P. Grendze, *J. Am. Chem. Soc.*, 1986, **108**, 6004–6011.

40 A. E. Tschitschibabin, *Chem. Ber.*, 1907, **40**, 1810.
41 Y. Ni, F. Gordillo-Gámez, M. P. Alvarez, Z. Nan, Z. Li, S. Wu, Y. Han, J. Casado and J. Wu, *J. Am. Chem. Soc.*, 2020, **142**, 12730–12742.
42 A. Shimizu, Y. Hirao, K. Matsumoto, H. Kurata, T. Kubo, M. Uruichib and K. Yakushi, *Chem. Commun.*, 2012, **48**, 5629–5631.
43 R. Huang, H. Phan, T. S. Herng, P. Hu, W. Zeng, S. Dong, S. Das, Y. Shen, J. Ding, D. Casanova and J. Wu, *J. Am. Chem. Soc.*, 2016, **138**, 10323–10330.
44 S. Dong, T. S. Herng, T. Y. Gopalakrishna, H. Phan, Z. L. Lim, P. Hu, R. D. Webster, J. Ding and C. Chi, *Angew. Chem., Int. Ed.*, 2016, **55**, 9316–9320.
45 G. E. J. L. Rudebusch, J. L. Zafra, K. Jorner, K. Fukuda, J. L. Marshall, I. Arrechea-Marcos, G. L. Espejo, R. Ponce Ortiz, C. J. Gomez-Garcia, L. N. Zakharov, M. Nakano, H. Ottosson, J. Casado and M. M. Haley, *Nat. Chem.*, 2016, **8**, 753–759.
46 A. Konishi, Y. Hirao, M. Nakano, A. Shimizu, E. Botek, B. Champagne, D. Shiomi, K. Sato, T. Takui, K. Matsumoto, H. Kurata and T. Kubo, *J. Am. Chem. Soc.*, 2010, **132**, 11021–11023.
47 A. Konishi, Y. Hirao, K. Matsumoto, H. Kurata, R. Kishi, Y. Shigeta, M. Nakano, K. Tokunaga, K. Kamada and T. Kubo, *J. Am. Chem. Soc.*, 2013, **135**, 1430–1437.
48 M. R. Ajayakumar, Y. Fu, J. Ma, F. Hennersdorf, H. Komber, J. J. Weigand, A. Alfonsov, A. A. Popov, R. Berger, J. Liu, K. Müllen and X. Feng, *J. Am. Chem. Soc.*, 2018, **140**, 6240–6244.
49 Y. Ni, T. Y. Gopalakrishna, H. Phan, T. S. Herng, S. Wu, Y. Han, J. Ding and J. Wu, *Angew. Chem., Int. Ed.*, 2018, **130**, 9845–9849.
50 J.-J. Shen, Y. Han, S. Dong, H. Phan, T. S. Herng, T. Xu, J. Ding and C. Chi, *Angew. Chem., Int. Ed.*, 2021, **60**, 4464–4469.
51 C. Janiak, R. Weimann and F. Görlitz, *Organometallics*, 1997, **16**, 4933–4936.
52 N. Jux, K. Holczer and Y. Rubin, *Angew. Chem., Int. Ed. Engl.*, 1996, **35**, 1986–1990.
53 K. Ogawa, K. Komatsu and T. Kitagawa, *J. Org. Chem.*, 2011, **76**, 6095–6100.
54 Z. Zeng, Y. M. Sung, N. Bao, D. Tan, R. Lee, J. L. Zafra, B. S. Lee, M. Ishida, J. Ding, J. T. L. Navarrete, Y. Li, W. Zeng, D. Kim, K.-W. Huang, R. D. Webster, J. Casado and J. Wu, *J. Am. Chem. Soc.*, 2012, **134**, 14513–14525.
55 X. Lu, S. Lee, J. O. Kim, T. Y. Gopalakrishna, H. Phan, T. S. Herng, Z. Lim, Z. Zeng, J. Ding, D. Kim and J. Wu, *J. Am. Chem. Soc.*, 2016, **138**, 13048–13058.
56 K. Goto, T. Kubo, K. Yamamoto, K. Nakasuji, K. Sato, D. Shiomi, T. Takui, M. Kubota, T. Kobayashi, K. Yakusi and J. Ouyang, *J. Am. Chem. Soc.*, 1999, **121**, 1619–1620.
57 D. Small, V. Zaitsev, Y. Jung, S. V. Rosokha, M. Head-Gordon and J. K. Kochi, *J. Am. Chem. Soc.*, 2004, **126**, 13850–13858.
58 Z. Mou, K. Uchida, T. Kubo and M. Kertesz, *J. Am. Chem. Soc.*, 2014, **136**, 18009–18022.
59 T. Kubo, Y. Katada, A. Shimizu, Y. Hirao, K. Sato, T. Takui, M. Uruichi, K. Yakushi and R. C. Haddon, *J. Am. Chem. Soc.*, 2011, **133**, 14240–14243.
60 Q. Xiang, J. Guo, J. Xu, S. Ding, Z. Li, G. Li, H. Phan, Y. Gu, Y. Dang, Z. Xu, Z. Gong, W. Hu, Z. Zeng, J. Wu and Z. Sun, *J. Am. Chem. Soc.*, 2020, **142**, 11022–11031.
61 G. M. Coppinger, *J. Am. Chem. Soc.*, 1957, **79**, 501–502.
62 G. M. Coppinger, *Tetrahedron*, 1962, **18**, 61–65.
63 D. Sakamaki, S. Yano, T. Kobashi, S. Seki, T. Kurahashi, S. Matsubara, A. Ito and K. Tanaka, *Angew. Chem., Int. Ed.*, 2015, **54**, 8267–8270.
64 S. Arikawa, A. Shimizu and R. Shintani, *Angew. Chem., Int. Ed.*, 2019, **58**, 6415–6419.
65 T. Kushida, S. Shirai, N. Ando, T. Okamoto, H. Ishii, H. Matsui, M. Yamagishi, T. Uemura, J. Tsurumi, S. Watanabe, J. Takeya and S. Yamaguchi, *J. Am. Chem. Soc.*, 2017, **139**, 14336–14339.
66 D. T. Chase, A. G. Fix, S. J. Kang, B. D. Rose, C. D. Weber, Y. Zhong, L. N. Zakharov, M. C. Lonergan, C. Nuckolls and M. M. Haley, *J. Am. Chem. Soc.*, 2012, **134**, 10349–10352.
67 A. M. Zeidell, L. Jennings, C. K. Frederickson, Q. Ai, J. J. Dressler, L. N. Zakharov, C. Risko, M. M. Haley and O. D. Jurchescu, *Chem. Mater.*, 2019, **31**, 6962–6970.
68 T. Kubo, A. Shimizu, M. Sakamoto, M. Uruichi, K. Yakushi, M. Nakano, D. Shiomi, K. Sato, T. Takui, Y. Morita and K. Nakasuji, *Angew. Chem., Int. Ed.*, 2005, **44**, 6564–6568.
69 M. Chikamatsu, T. Mikami, J. Chisaka, Y. Yoshida, R. Azumi, K. Yase, A. Shimizu, T. Kubo, Y. Morita and K. Nakasuji, *Appl. Phys. Lett.*, 2007, **91**, 043506.
70 X. Shi, S. Lee, M. Son, B. Zheng, J. Chang, L. Jing, K.-W. Huang, D. Kim and C. Chi, *Chem. Commun.*, 2015, **51**, 13178–13180.
71 C. Zong, X. Zhu, Z. Xu, L. Zhang, J. Xu, J. Guo, Q. Xiang, Z. Zeng, W. Hu, J. Wu, R. Li and Z. Sun, *Angew. Chem., Int. Ed.*, 2021, **60**, 16230–16236.
72 T. Jousselin-Oba, M. Mamada, J. Marrot, A. Maignan, C. Adachi, A. Yassar and M. Frigoli, *J. Am. Chem. Soc.*, 2019, **141**, 9373–9381.
73 T. Takahashi, K. Matsuoka, K. Takimiya, T. Otsubo and Y. Aso, *J. Am. Chem. Soc.*, 2005, **127**, 8928–8929.
74 S. Handa, E. Miyazaki, K. Takimiya and Y. Kunugi, *J. Am. Chem. Soc.*, 2007, **129**, 11684–11685.
75 Q. Wu, R. Li, W. Hong, H. Li, X. Gao and D. Zhu, *Chem. Mater.*, 2011, **23**, 3138–3140.
76 N. Yanai, T. Mori, S. Shinamura, I. Osaka and K. Takimiya, *Org. Lett.*, 2014, **16**, 240–243.
77 T. Mori, N. Yanai, I. Osaka and K. Takimiya, *Org. Lett.*, 2014, **16**, 1334–1337.
78 J. L. Zafra, L. Qiu, N. Yanai, T. Mori, M. Nakano, M. P. Alvarez, J. T. L. Navarrete, C. J. Gólmez-García, M. Kertesz, K. Takimiya and J. Casado, *Angew. Chem., Int. Ed.*, 2016, **55**, 14563–14568.
79 A. F. Garito and A. J. Heeger, *Acc. Chem. Res.*, 1974, **7**, 232–240.
80 J. Ferraris, D. O. Cowan, V. Walatka and J. H. Perlstein, *J. Am. Chem. Soc.*, 1973, **95**, 948–949.

81 H. Alves, A. S. Molinari, H. Xie and A. F. Morpurgo, *Nat. Mater.*, 2008, **7**, 574–580.
82 Y. Ji, L. Long and Y. Zheng, *Mater. Chem. Front.*, 2020, **4**, 3433–3443.
83 Y. Zheng, M.-S. Miao, G. Dantelle, N. D. Eisenmenger, G. Wu, I. Yavuz, M. L. Chabinyc, K. N. Houk and F. Wudl, *Adv. Mater.*, 2015, **27**, 1718–1723.
84 Y. Zhang, Y. Zheng, H. Zhou, M.-S. Miao, F. Wudl and T.-Q. Nguyen, *Adv. Mater.*, 2015, **27**, 7412–7419.
85 D. Yuan, Y. Guo, Y. Zeng, Q. Fan, J. Wang, Y. Yi and X. Zhu, *Angew. Chem., Int. Ed.*, 2019, **58**, 4958–4962.
86 D. Yuan, D. Huang, S. M. Rivero, A. Carreras, C. Zhang, Y. Zou, X. Jiao, C. R. McNeill, X. Zhu, C.-A. Di, D. Zhu, D. Casanova and J. Casado, *Chem*, 2019, **5**, 964–976.
87 K. Yang, X. Zhang, A. Harbuzaru, L. Wang, Y. Wang, C. Koh, H. Guo, Y. Shi, J. Chen, H. Sun, K. Feng, M. C. R. Delgado, H. Y. Woo, R. P. Ortiz and X. Guo, *J. Am. Chem. Soc.*, 2020, **142**, 4329–4340.
88 K. Uchida, Z. Mou, M. Kertesz and T. Kubo, *J. Am. Chem. Soc.*, 2016, **138**, 4665–4672.
89 X. Chi, M. E. Itkis, B. O. Patrick, T. M. Barclay, R. W. Reed, R. T. Oakley, A. W. Cordes and R. C. Haddon, *J. Am. Chem. Soc.*, 1999, **121**, 10395–10402.
90 X. Chi, M. E. Itkis, K. Kirschbaum, A. A. Pinkerton, R. T. Oakley, A. W. Cordes and R. C. Haddon, *J. Am. Chem. Soc.*, 2001, **123**, 4041–4048.
91 M. E. Itkis, X. Chi, A. W. Cordes and R. C. Haddon, *Science*, 2002, **296**, 1443–1445.
92 S. K. Pal, M. E. Itkis, F. S. Tham, R. W. Reed, R. T. Oakley and R. C. Haddon, *Science*, 2005, **309**, 281–284.
93 S. K. Mandal, S. Samanta, M. E. Itkis, D. W. Jensen, R. W. Reed, R. T. Oakley, F. S. Tham, B. Donnadieu and R. C. Haddon, *J. Am. Chem. Soc.*, 2006, **128**, 1982–1994.
94 Y. Morita1, S. Nishida, T. Murata, M. Moriguchi, A. Ueda, M. Satoh, K. Arifuku, K. Sato and T. Takui, *Nat. Mater.*, 2011, **10**, 947–951.
95 Y. Morita, T. Murata, A. Ueda, C. Yamada, Y. Kanzaki, D. Shiomi, K. Sato and T. Takui, *Bull. Chem. Soc. Jpn.*, 2018, **91**, 922–931.
96 T. Murata, C. Yamada, K. Furukawa and Y. Morita, *Commun. Chem.*, 2018, **1**, 47.
97 M. Souto, H. Cui, M. Peña-Álvarez, V. G. Baonza, H. O. Jeschke, M. Tomic, R. Valentí, D. Blasi, I. Ratera, C. Rovira and J. Veciana, *J. Am. Chem. Soc.*, 2016, **138**, 11517–11525.
98 V. Gamero, D. Velasco, S. Latorre, F. López-Calahorra, E. Brillasc and L. Juliá, *Tetrahedron Lett.*, 2006, **47**, 2305–2309.
99 Q. Peng, A. Obolda, M. Zhang and F. Li, *Angew. Chem., Int. Ed.*, 2015, **54**, 7091–7095.
100 X. Ai, E. W. Evans, S. Dong, A. J. Gillett, H. Guo, Y. Chen, T. J. H. Hele, R. H. Friend and F. Li, *Nature*, 2018, **563**, 536–540.
101 A. Abdurahman, T. J. H. Hele, Q. Gu, J. Zhang, Q. Peng, M. Zhang, R. H. Friend, F. Li and E. W. Evans, *Nat. Mater.*, 2020, **19**, 1224–1229.
102 H. Guo, Q. Peng, X. Chen, Q. Gu, S. Dong, E. W. Evans, A. J. Gillett, X. Ai, M. Zhang, D. Credgington, V. Coropceanu, R. H. Friend, J. L. Bredas and F. Li, *Nat. Mater.*, 2019, **18**, 977–984.
103 X. Ai, Y. Chen, Y. Feng and F. Li, *Angew. Chem., Int. Ed.*, 2018, **57**, 2869–2873.
104 Y. Hattori, T. Kusamoto and H. Nishihara, *RSC Adv.*, 2015, **5**, 64802–64805.
105 Y. Hattori, T. Kusamoto and H. Nishihara, *Angew. Chem., Int. Ed.*, 2015, **54**, 3731–3734.
106 T. Kusamoto, S. Kimura, Y. Ogino, C. Ohde and H. Nishihara, *Chem. – Eur. J.*, 2016, **22**, 17725–17733.
107 T. Kusamoto, Y. Hattori, A. Tanushi and H. Nishihara, *Inorg. Chem.*, 2015, **54**, 4186–4188.
108 S. Kimura, H. Uchida, T. Kusamoto and H. Nishihara, *Dalton Trans.*, 2019, **48**, 7090–7093.
109 S. Kimura, R. Matsuoka, S. Kimura, H. Nishihara and T. Kusamoto, *J. Am. Chem. Soc.*, 2021, **143**, 5610–5615.
110 E. Moulin, F. Niess, M. Maaloum, E. Buhler, I. Nyrkova and N. Giuseppone, *Angew. Chem., Int. Ed.*, 2010, **49**, 6974–6978.
111 J. J. Armao, M. Maaloum, T. Ellis, G. Fuks, M. Rawiso, E. Moulin and N. Giuseppone, *J. Am. Chem. Soc.*, 2014, **136**, 11382–11388.
112 Y. Mu, Y. Liu, H. Tian, D. Ou, L. Gong, J. Zhao, Y. Zhang, Y. Huo, Z. Yang and Z. Chi, *Angew. Chem., Int. Ed.*, 2021, **60**, 6367–6371.
113 X. Zhao, J. Gong, P. Alam, C. Ma, Y. Wang, J. Guo, Z. Zeng, Z. He, H. H. Y. Sung, I. D. Williams, K. S. Wong, S. Chen, J. W. Y. Lam, Z. Zhao and B. Z. Tang, *CCS Chem.*, 2021, DOI: 10.31635/ccschem.021.202101192.
114 Y. Yang, J. Wang, D. Li, J. Yang, M. Fang and Z. Li, *Adv. Mater.*, 2021, **33**, 2104002.